NATIONAL ADVISORY COMMITTEE FOR AERONAUTICS

TECHNICAL NOTE

No. 1810

COMPARISON BETWEEN PREDICTED AND OBSERVED PERFORMANCE OF GAS-TURBINE STATOR BLADE DESIGNED FOR FREE-VORTEX FLOW

By M. C. Huppert and Charles MacGregor

Lewis Flight Propulsion Laboratory
Cleveland, Ohio

Washington
April 1949

NATIONAL ADVISORY COMMITTEE FOR AERONAUTICS

TECHNICAL NOTE NO. 1810

COMPARISON BETWEEN PREDICTED AND OBSERVED PERFORMANCE OF GAS-TURBINE STATOR BLADE DESIGNED FOR FREE-VORTEX FLOW

By M. C. Huppert and Charles MacGregor

SUMMARY

A comparison was made between the calculated design performance of a gas-turbine stator blade and its performance in a sector of an annular cascade tunnel. Information was obtained with regard to the three-dimensional effects that occur; the influence these effects have upon various performance parameters are presented.

The gas velocities on the blade surfaces were computed by the stream-filament method and compared with the experimental values. The calculated values satisfactorily agree with the experimental values.

The design conditions of free-vortex flow were not obtained. The experimental tangential velocities were greater than the design values at the tip of the blade but lower than the design values at the root of the blade.

INTRODUCTION

In the design of gas-turbine stator blades, compromises are generally made between aerodynamic considerations and such practical considerations as service life and cost of manufacture. In order for a turbine to perform efficiently and to meet design conditions of power and weight flow of gas, however, the blades must be designed by a procedure that accurately predicts blade performance.

The blade profiles are generally designed according to two-dimensional-flow theory. The velocity distribution along the blade surface must be such that flow separation or excessively high local velocities will be avoided. This velocity distribution may be determined by an incompressible potential-flow theory, which is applicable for any solidity or camber of the blades (references 1 to 4).

These methods, however, do not consider compressibility and are mathematically complex. Stream-filament theories that consider compressibility may be used to design blades of high solidity. These methods involve graphical integration of the flow equations (reference 5). Satisfactory experimental verification of either the potential-flow theories or of stream-filament theories have previously been lacking.

The design performance of turbine stator blades based on free-vortex flow as measured in a sector of an annular cascade tunnel was determined at the NACA Lewis laboratory. The blade-surface velocities were calculated by an approximation, which was developed at the NACA Lewis laboratory, of the stream-filament method of reference 5 and are compared with experimental values.

SYMBOLS

The following symbols are used in this report:

C	curvature, (1/ft, unless otherwise noted)
c_p	specific heat at constant pressure, (ft-lb/(slug)($^\circ$R))
c_v	specific heat at constant volume, (ft-lb/(slug)($^\circ$R))
exp	base of Napierian logarithmic system e raised to power in parentheses following exp
n	distance from blade suction surface to any point on velocity-potential line, (ft, unless otherwise noted)
n_o	length of velocity potential line from suction surface to pressure surface, (ft, unless otherwise noted)
P	pressure, (lb/sq ft absolute)
r	radius, (ft, unless otherwise noted)
S	blade-surface length, (ft, unless otherwise noted)
T	temperature, ($^\circ$R)
V	velocity, (ft/sec)
V_{cr}	critical velocity, $\sqrt{\frac{\gamma-1}{\gamma+1} 2c_p T_t}$, (ft/sec)

W	weight of gas flowing across velocity-potential line per unit depth, (slug/sec)
$\sqrt{Z}$	$\frac{V}{\sqrt{2c_pT_t}} = \sqrt{\frac{\gamma-1}{\gamma+1}}\ \frac{V}{V_{cr}}$
α	angle between normal to cascade axis and flow direction of gas, (deg)
Γ	circulation, (sq ft/sec)
γ	ratio of specific heats, c_p/c_v
ν	local deflection angle, (deg)
ρ	density, (slugs/cu ft)
τ	blade pitch, (ft, unless otherwise noted)
ϕ	velocity potential, (sq ft/sec)
ψ	stream function (slugs/sec)

Subscripts:

0	ambient static conditions
1	suction (convex) surface
2	pressure (concave) surface
e	cascade exit
i	cascade entrance
m	value at point of average streamline curvature
r	component in radial direction
s	static conditions
t	stagnation conditions
u	component in tangential direction
x	component in axial direction

Parameters:

a $\quad \dfrac{n_o C_1}{2}$

b $\quad -\dfrac{C_1}{\Delta C}$

f $\quad \sqrt{Z_m}(1 - Z_m)^{\frac{2-\gamma}{\gamma-1}} \left[1 + Z_m \left(\dfrac{2-\gamma}{\gamma-1}\right)\right]$

$F(t_1)$ $\quad \displaystyle\int_o^{t_1} \exp\,(t^2)dt$

$F(t_2)$ $\quad \displaystyle\int_o^{t_2} \exp\,(t^2)dt$

g $\quad \dfrac{Z_m^{3/2}}{\gamma-1}(1-Z_m)^{\frac{2-\gamma}{\gamma-1}}$

J $\quad \displaystyle\int_{C_1}^{C_2} \exp\left[-\frac{n_o}{2\Delta C}(C^2 - C_m^2)\right]\frac{dC}{\Delta C}$

K $\quad \displaystyle\int_{C_1}^{C_2} \exp\left[-\frac{3n_o}{2\Delta C}(C^2 - C_m^2)\right]\frac{dC}{\Delta C}$

t $\quad C\sqrt{-\dfrac{n_o}{2\Delta C}}$

y $\quad \sqrt{-\dfrac{n_o \Delta C}{2}}$

μ $\quad \dfrac{W}{\rho_t n_o \sqrt{2c_p T_t}}$

$\frac{\rho_s V_x}{\rho_t V_{cr}}$ weight-flow parameter

$\frac{r}{P_t}\frac{dP_s}{dr}$ radial pressure-gradient parameter

$\frac{\rho_s}{\rho_t}\left(\frac{V_u}{V_{cr}}\right)^2$ centrifugal-force parameter

$\frac{r}{V_{cr}}\frac{\rho_s}{\rho_t}\frac{dV_r}{dt}$ radial-acceleration parameter

BLADE DESIGN

The turbine stator considered was designed for the following conditions: inlet-gas pressure, 8200 pounds per square foot; inlet-gas temperature, 1900° R, gas flow, 40.4 pounds per second; power output, 4300 horsepower, and rotor-blade speed at the 10.35-inch radius, 1000 feet per second. The weight-flow parameter, critical velocity ratio, and gas-flow angle at three radial stations are listed in the following table:

Station	Radius r (in.)	Weight-flow parameter $\left(\frac{\rho_s V_x}{\rho_t V_{cr}}\right)_i$	Weight-flow parameter $\left(\frac{\rho_s V_x}{\rho_t V_{cr}}\right)_e$	Critical velocity ratio $\left(\frac{V}{V_{cr}}\right)_e$	Gas discharge angle α_e (deg)
Root	9.3	0.212	0.233	0.878	67.8
Pitch	10.35	.212	.249	.800	65.6
Tip	11.5	.212	.260	.737	63.3

These values were computed on the assumptions of radial equilibrium, constant gas energy and entropy, and free-vortex flow from root to tip. These assumptions result in theoretically constant axial velocity at all radii (reference 6). Flow-area blockage due to boundary-layer development at the blade root and tip was considered by assuming, in accordance with the experimental data of reference 6, a boundary-layer-displacement thickness of 0.3 and 0.1 inch at the inner and outer shroud, respectively.

In establishing a velocity distribution over the blade surface, flow acceleration over as much of the blade surface as possible is considered desirable. Thus, blade shapes at three radial stations, root, pitch, and tip (table I) were designed with the stream-filament theory developed in appendix A by the procedure outlined in appendix B. Values of local deflection angle at cascade entrance, ν_i and local deflection angle at cascade exit ν_e of 5° and 2°, respectively, were used at all radii. The values were graphically obtained from previous designs based on potential-flow theory (reference 3).

The blade coordinates and other dimensions are shown in table I. Blade shapes for a typical blade section with the velocity-potential lines used in calculating surface velocities are shown in figure 1. The calculated surface velocities are plotted against blade-surface length in figure 2.

APPARATUS AND PROCEDURE

The investigation was conducted with five blades mounted in a sector of an annular cascade to simulate three-dimensional flow. A sketch of the experimental equipment is shown in figure 3.

The experimental conditions were different from the design conditions in that the blades were designed for an inlet-gas temperature of 1900° R and the experiments were conducted at an inlet-gas temperature of 580° R. The Reynolds number (based on the pitch of the blade) for the turbine blades at design conditions was 600,000; whereas, for the cascade experiments, the Reynolds number was 800,000. The effect of this difference was considered small. The blades were, however, investigated at the design value of critical velocity ratio V/V_{cr} near the pitch section of the blade.

The pressure distribution about the center blade of the cascade was measured with 36 static-pressure tubes of 0.030-inch diameter located as indicated in table II. Pressures were measured with mercury manometers.

A survey probe, which is shown in the enlarged portion of figure 3, was used to determine the angle at which the gas discharged from the cascade of blades. The gas angle, measured from the axial direction, was read on a protractor. The center tube of the probe was used to indicate the stagnation pressure; the static pressure was read by static-pressure holes located 9 diameters downstream of the tip of the probe. The position of the end of the

probe was varied in the discharge field by manipulation of the traversing mechanism. The static pressures at the inner and outer shrouds were read by wall taps located midway between blades in line with the trailing edge.

A preliminary survey of the tunnel was conducted to assure a uniform pressure field upstream of the blades. The stagnation- and static-pressure distribution across the tunnel along the survey paths (indicated in fig. 4) is shown in figure 5 for a plane 1.5 chord lengths upstream of the blades. Inasmuch as no boundary-layer-control slots were provided, the boundary-layer development upstream of the blades along the inner and outer shrouds was investigated. The approach was long enough to provide uniform flow and short enough to prevent excessive boundary-layer growth, as seen in figure 5. The variation of weight-flow parameter at the cascade entrance with the ratio of stagnation pressure at the cascade entrance to ambient static pressure is shown in figure 6. The test condition is indicated.

The following measurements were made to determine blade performance:

1. Stagnation and static-pressure surveys, both upstream and downstream of blades

2. Stagnation upstream temperature (held constant at 580° R)

3. Static-pressure distribution about center blade of cascade

4. Survey of angle of discharge of blade

The downstream surveys were made in a plane 0.1 chord length behind the blades. The surveys were made close to the blades because the inner and outer shrouds extended only 1 chord length downstream of the blades.

RESULTS AND DISCUSSION

The stagnation and static pressures at simulated design conditions in a survey plane 0.1 chord length downstream of cascade at points midway between blades at a number of radial stations are shown in figure 7. The construction of the survey equipment limited the positioning of the probe to radii 0.3 inch less than that of the outer shroud. The data of figure 7 are plotted as the ratio of stagnation-to-static pressure in figure 8. The design value of

pressure ratio at any radius is the pressure ratio that would be obtained with radial equilibrium of pressures and free-vortex flow at design conditions. The experimental results show a pressure ratio at the root 2 percent lower than the design value and a pressure ratio at the tip 4 percent greater than the design value.

Discharge angle. - The gas-discharge angle measured from the axial direction at a number of radial stations in a plane 0.1 chord downstream of the blades is shown in figure 9(a). In general, the air was turned approximately 1° more than the design value. The gas was considerably overturned in the boundary layer near the inner shroud. This region of severe overturn is followed by an adjacent region at a larger radius in which the gases were turned to the design leaving angle. Near the outer shroud the gases were slightly underturned.

Although no data were taken at the outer shroud, the gases were probably overturned in this region. The overturning near the inner shroud is probably caused by secondary flow from the high-pressure region on the pressure surface of the blade to the low-pressure region on the suction surface as explained in reference 6.

The variation in discharge angle in the circumferential direction at the 10.35-inch radius is shown in figure 9(b). The gases near the suction surface of a blade were turned about 8° more than the gases near the pressure surface of the adjacent blade. Inasmuch as the included angle between suction and pressure surfaces at the trailing edge is 10°, some difference between discharge angle near the two surfaces was to be expected.

Vane-surface-velocity distribution. - The experimental- and calculated-design-velocity distribution about the root, pitch, and tip sections of the blade are shown in figure 2. The experimental values of velocity on the blade surface were computed from experimental values of static pressure, assuming no loss in total pressure in the region outside the boundary layer on the blade surface. With this assumption, the surface velocity at a point on the blade surface is related to the static pressure at the same point as follows:

$$\frac{V}{V_{cr}} = \sqrt{\frac{\gamma+1}{\gamma-1}\left[1 - \left(\frac{P_s}{P_t}\right)^{\frac{\gamma-1}{\gamma}}\right]}$$

where the total pressure P_t is measured upstream of the blade row.

In general, the experimental velocities are higher than design values on the pressure surface and lower on the suction surface. The differences are more pronounced at the root and tip sections than at the pitch section; however, these sections are at the edge of the boundary layers on the inner and outer shrouds. The shear stresses in the boundary layer cause an increase in entropy and deviation from the theoretical velocities.

Tangential- and axial-velocity distribution. - The gas-discharge-velocity components were computed from the pressure ratios of figure 8 and the discharge angles of figure 9(a), assuming that the radial component of velocity is small enough to be neglected.

The experimental and design values of critical velocity ratio V/V_{cr} are plotted against radius in figure 10(a). The measured values are 3 percent higher than design near the blade tip and 3 percent lower than design near the blade root.

The measured values of tangential component of critical velocity ratio V_u/V_{cr} are 3 percent higher than design near the blade tip and 3 percent lower near the blade root, as shown in figure 10(b). Vortex distribution of V_u/V_{cr} was not obtained; but inasmuch as the values are, in general, greater than design values, the turbine power will probably exceed the design power by about 2 percent if the rotor is assumed to perform as designed.

Constant axial velocity was not achieved (fig. 11(a)); the experimental values were about 6 percent lower than the design value at the 10-inch radius and 6 percent higher near the blade tip.

The weight-flow parameter $\frac{\rho_s V_x}{\rho_t V_{cr}}$ obtained from the data is compared with the design values in figure 11(b). This parameter is quite close to the design value at the blade sections at which the blade-surface-pressure distributions were obtained; at the 10-inch radius, however, this parameter is 6 percent lower than the design value. Although no accurate computation of the experimental boundary-layer thicknesses at the blade root and tip can be made because of insufficient data describing conditions near the tunnel shrouds, the check between design weight flow and experimental weight flow is considered close enough to say that the design allowance for boundary-layer growth at the shroud was adequate. The principal reason that vortex flow was not achieved is because radial equilibrium of pressure was not attained. The heavy boundary layer at the inner shroud also tends to deflect the air toward the outer shroud and distorts the flow near the inner shroud.

Radial-equilibrium consideration. - As stated in the discussion of blade design, the blades were designed on the assumption of radial equilibrium of pressure. This condition may be stated as follows:

$$\frac{dP_s}{dr} = \frac{\rho_s V_u^2}{r}$$

This equation states that the centrifugal force on the air particles is balanced by a pressure difference across the particles. However, because radial flow must take place as the gases pass through the passage between blades if the exit axial velocity is to remain constant at all radii, the gas will be accelerated radially outward. These radial acceleration forces can be considered by writing

$$\frac{dP_s}{dr} = \frac{\rho_s V_u^2}{r} - \rho_s \frac{dV_r}{dt}$$

This expression may be written in dimensionless form for convenience as

$$\frac{\gamma+1}{2\gamma} \frac{r}{P_t} \frac{dP_s}{dr} = \frac{\rho_s}{\rho_t} \left(\frac{V_u}{V_{cr}}\right)^2 - \frac{r}{V_{cr}^2} \frac{\rho_s}{\rho_t} \frac{dV_r}{dt}$$

The design assumption in effect neglected the radial acceleration of velocity term involving $\frac{dV_r}{dt}$.

The magnitude of the radial-acceleration parameter involving the rate of change of radial velocity with time at the experimental conditions is shown in figure 12. The radial-pressure-gradient parameter $\frac{r}{P_t} \frac{dP_s}{dr}$ was calculated by graphically differentiating the lower curve of figure 7. The centrifugal-force parameter $\frac{\rho_s}{\rho_t}\left(\frac{V_u}{V_{cr}}\right)^2$ was computed from figures 10(b) and 7 by assuming isentropic flow.

The radial-acceleration parameter $\frac{r}{V_{cr}^2} \frac{\rho_s}{\rho_t} \frac{dV_r}{dt}$ was then evaluated by subtracting $\frac{\gamma+1}{2\gamma} \frac{r}{P_t} \frac{dP_s}{dr}$ from $\frac{\rho_s}{\rho_t} \left(\frac{V_u}{V_{cr}}\right)^2$. Although

$\frac{r}{V_{cr}^2}\frac{dV_r}{dt}$ is nearly as large as $\frac{r}{P_t}\frac{dP_s}{dr}$ near the blade tip, the effect on $\frac{\rho_s}{\rho_t}\left(\frac{V_u}{V_{cr}}\right)^2$ was small (about 4 percent) and the deviation from free-vortex flow was small.

SUMMARY OF RESULTS

From a comparison of the calculated design performance and the experimental performance of a gas-turbine stator blade, the following results were obtained:

1. The stream-filament theory is adequate to determine gas velocities on the surface of high-solidity blades. For the blades investigated, the calculated surface velocities satisfactorily agreed with the experimental values.

2. The experimental value of tangential component of critical velocity ratio was 3 percent greater than the design value at the blade tip and 3 percent less than the design value at the blade root. These deviations were caused by lack of radial equilibrium of pressures at 0.1 chord downstream of the turbine blades and the thick boundary layer at the inner shroud.

3. Constant axial velocity at all radii was not achieved. The experimental axial velocity was 6 percent higher than the design axial velocity near the blade tip.

4. Although the radial-acceleration forces were large, the deviation from free-vortex flow was small.

Lewis Flight Propulsion Laboratory,
National Advisory Committee for Aeronautics,
Cleveland, Ohio, September 13, 1948.

APPENDIX A

STREAM-FILAMENT THEORY

The two-dimensional flow between curved surfaces may be studied by the stream-filament theory if the channel length is great compared to its width. This method consists in combining the conditions of irrotationality of flow with the principle of continuity of flow.

Determination of velocity variation across channel. - In the general case of the motion of a compressible, frictionless, perfect gas between curved surfaces (fig. 13), at any point in the channel the fluid rotates about an instantaneous center at radius r with velocity V. Inasmuch as the fluid is considered irrotational,

$$\frac{dV}{dn} = -\frac{V}{r} = -CV \tag{1}$$

The derivative is negative, inasmuch as the positive direction is chosen as that from the suction surface to the pressure surface.

The curvature of the streamline is assumed to vary linearly from the suction surface to the pressure surface and is considered positive if the center of curvature is below the surface.

$$C = C_1 + \frac{C_2 - C_1}{n_o} n \tag{2}$$

$$= C_1 + \frac{\Delta C}{n_o} n \tag{3}$$

Then

$$dC = \frac{\Delta C}{n_o} dn \tag{4}$$

If equation (1) is rewritten in terms of curvature and equation (4) is used,

$$\frac{dV}{V} = -\frac{n_o}{\Delta C} C\, dC \tag{5}$$

When equation (5) is integrated,

$$\log_e V = - \frac{n_o C^2}{2\Delta C} + \text{constant} \tag{6}$$

or

$$\frac{V}{V_m} = \exp \left[- \frac{n_o}{2\Delta C} (C^2 - C_m^2) \right] \tag{7}$$

where V and V_m represent the velocity at any two points along the potential line.

Evaluation of velocity from mass flow. - If the velocity at any point along a potential line is known, then the rest of the velocities along the line can be determined, as indicated in equation (7). From the use of the continuity equation, the velocity at one point may be determined.

The differential quantity of mass flow per unit depth of channel

$$dW = \rho_s V \, dn \tag{8}$$

or in terms of density and temperature at stagnation

$$dW = \rho_t \left(1 - \frac{V^2}{2 c_p T_t} \right)^{\frac{1}{\gamma - 1}} V \, dn \tag{9}$$

Now, let

$$Z = \frac{V^2}{2 c_p T_t} \tag{10}$$

then,

$$\frac{dW}{\rho_t \sqrt{2\, c_p\, T_t}\, n_o} = (1 - Z)^{\frac{1}{\gamma-1}}\, \sqrt{Z}\, \frac{dn}{n_o} \tag{11}$$

$$(1 - Z)^{\frac{1}{\gamma-1}} = (1 - Z_m - Z + Z_m)^{\frac{1}{\gamma-1}}$$

$$= (1 - Z_m)^{\frac{1}{\gamma-1}} \left(1 - \frac{Z - Z_m}{1 - Z_m}\right)^{\frac{1}{\gamma-1}} \tag{12}$$

where

$$Z_m = \frac{V_m^2}{2\, c_p\, T_t} \tag{13}$$

The second term in equation (12) may be expanded by the binomial theorem, choosing $\sqrt{Z_m}$ at the point of average streamline curvature (channel center) so that $Z - Z_m$ will be small, and neglecting all but the first two terms of the expansion, then

$$(1 - Z)^{\frac{1}{\gamma-1}} = (1 - Z_m)^{\frac{1}{\gamma-1}} \left[1 + \frac{1}{\gamma-1}\left(\frac{Z_m}{1 - Z_m}\right) - \frac{1}{\gamma-1}\left(\frac{Z}{1 - Z_m}\right)\right]$$

$$= (1 - Z_m)^{\frac{2-\gamma}{\gamma-1}} \left[1 + Z_m\left(\frac{2-\gamma}{\gamma-1}\right) - \frac{Z}{\gamma-1}\right] \tag{14}$$

Let

$$f = \sqrt{Z_m}\, (1 - Z_m)^{\frac{2-\gamma}{\gamma-1}} \left[1 + Z_m\left(\frac{2-\gamma}{\gamma-1}\right)\right] \tag{15}$$

and

1026

$$g = \frac{Z_m^{3/2}}{\gamma-1}\left(1 - Z_m\right)^{\frac{2-\gamma}{\gamma-1}} \tag{16}$$

Then,

$$(1 - Z)^{\frac{1}{\gamma-1}} = \frac{f}{\sqrt{Z_m}} - g\frac{Z}{Z_m^{3/2}} \tag{17}$$

Then equation (11) becomes

$$\frac{dW}{\rho_t\, n_o \sqrt{2\, c_p\, T_t}} = \left[f\sqrt{\frac{Z}{Z_m}} - g\left(\frac{Z}{Z_m}\right)^{3/2}\right]\frac{dn}{n_o} \tag{18}$$

Let

$$\mu = \frac{1}{\rho_t\, n_o \sqrt{2\, c_p\, T_t}} \int_0^W dW$$

$$= \frac{W}{\rho_t\, n_o \sqrt{2\, c_p\, T_t}} \tag{19}$$

If equation (18) is integrated,

$$\mu = \int_0^{n_o} f\sqrt{\frac{Z}{Z_m}}\frac{dn}{n_o} - \int_0^{n_o} g\left(\frac{Z}{Z_m}\right)^{3/2}\frac{dn}{n_o} \tag{20}$$

but

$$\sqrt{\frac{Z}{Z_m}} = \frac{V}{V_m}$$

and from equations (7) and (4)

$$\sqrt{\frac{Z}{Z_m}} = \exp\left[-\frac{n_o}{2\Delta C}\left(C^2 - C_m{}^2\right)\right] \tag{21}$$

let

$$J = \int_{C_1}^{C_2} \exp\left[-\frac{n_o}{2\Delta C}\left(C^2 - C_m{}^2\right)\right]\frac{dC}{\Delta C} \tag{22}$$

and

$$K = \int_{C_1}^{C_2} \exp\left[-\frac{3n_o}{2\Delta C}\left(C^2 - C_m{}^2\right)\right]\frac{dC}{\Delta C} \tag{23}$$

Then equation (20) becomes

$$\mu = fJ - gK$$

or

$$f = g\frac{K}{J} + \frac{\mu}{J} \tag{24}$$

Equations (22) and (23) may be evaluated for J and K for $C_1 > C_2$ by letting

$$t^2 = -\frac{n_o C^2}{2\Delta C} \tag{25}$$

Then,

$$C = t\sqrt{-\frac{2\Delta C}{n_o}}$$

and

$$\frac{dC}{\Delta C} = -\,dt\sqrt{\frac{-2}{\Delta C\, n_o}}$$

Then,

$$J = \frac{\exp\left(\frac{n_o C_m^2}{2\Delta C}\right)}{\sqrt{-\frac{n_o \Delta C}{2}}} \int_{t_2}^{t_1} \exp\left(-\frac{n_o C^2}{2\Delta C}\right) dt$$

$$= \frac{\exp\left[-t_m^2\right]}{\sqrt{-\frac{\Delta C\, n_o}{2}}} \int_{t_2}^{t_1} \exp\left(t^2\right) dt \qquad (26)$$

and

$$K = \frac{\exp\left[-3\, t_m^2\right]}{\sqrt{-\frac{3}{2}\Delta C\, n_o}} \int_{\sqrt{3}\, t_2}^{\sqrt{3}\, t_1} \exp\left(3t^2\right)\, d\sqrt{3}t \qquad (27)$$

The terms t_1 and t_2 are known from the channel dimensions and a table of $\int_0^x \exp(t^2)dt$ can be found in reference 7.

Evaluation of velocity at channel center. - The factors f and g are functions only of $\sqrt{Z_m}$ and γ (equations (15) and (16)). Thus, for given values of $\sqrt{Z_m}$ and γ, curves of f plotted against $\sqrt{Z_m}$ and g can be made, as shown in figure 14. In order to evaluate $\sqrt{Z_m}$, a line is drawn at $\tan^{-1}\frac{K}{J}$ intersecting the ordinate of the plot of f against g at $\frac{\mu}{J}$ (fig. 14). The line will, in general, intersect the curve at two points, one intersection corresponding to the subsonic solution and the other, the supersonic solution. If the line is tangent to the curve, the channel is choked. If the line lies above the curve, no solution exists inasmuch as μ is larger than physically possible. The value of $\sqrt{Z_m}$ is then found by drawing a horizontal line from the subsonic or supersonic intersection point, whichever is desired, to the curve of f against $\sqrt{Z_m}$; then $\sqrt{Z_m}$ is read on the abscissa as shown in figure 14.

The incompressible value of $\sqrt{Z_m}$ is determined by setting $g = 0$ that is,

$$\frac{\mu}{J} = f = \sqrt{Z_m} \qquad \left(\frac{\mu}{J} < 0.25\right)$$

Then

$$\frac{W}{\rho_t \, n_o \, J} = V_m$$

Inasmuch as the flow is considered incompressible

$$\rho_t = \rho_s$$

$$V_m = \frac{W}{\rho_s \, n_o \, J}$$

Evaluation of J and K. - A chart for the evaluation of J and K/J to be used in finding $\sqrt{Z_m}$ would be a simplification over evaluation from tables. A chart can be constructed where J and K/J are functions of the surface curvature and channel width, inasmuch as from equation (26)

$$J_1 = \frac{\exp\left(-t_m^2\right)}{\sqrt{-\frac{\Delta C \, n_o}{2}}} \left[F\left(t_1\right) - F\left(t_2\right)\right] \tag{28}$$

Let

$$y = \sqrt{-\frac{n_o \, \Delta C}{2}} \tag{29}$$

Then,

$$t_m = \frac{-y}{\Delta C}\left(\frac{C_2 + C_1}{2}\right) \tag{30}$$

and

$$F(t_1) = F\left(t_m + \frac{y}{2}\right) \tag{31}$$

$$F(t_2) = F\left(t_m - \frac{y}{2}\right) \tag{32}$$

These functions may be expanded in a Taylor's series.

$$F(t_1) - F(t_2) = 2\left[\left(\frac{y}{2}\right) F'(t_m) + \left(\frac{y}{2}\right)^3 \frac{F'''(t_m)}{3!} + \ldots + \left(\frac{y}{2}\right)^n \frac{F^n(t_m)}{n!}\right] \tag{33}$$

where n is an odd positive integer and

$$F'(t_m) = \exp(t_m^2)$$

$$F'''(t_m) = (2 + 4\,t_m^2) \exp(t_m^2)$$

By use of the first five terms of the Taylor's series,

$$J = 1 + \frac{y^2}{12}(1 + 2\,t_m^2) + \frac{y^4}{480}(3 + 12\,t_m^2 + 4\,t_m^4) \tag{34}$$

Now, let

$$a = t_1\,y = \frac{n_o\,C_1}{2} \tag{35}$$

$$b = \frac{t_1}{y} = -\frac{C_1}{\Delta C} \tag{36}$$

Then,

$$t_m^2 = \frac{a}{4b}(2b - 1)^2$$

and equation (34) becomes

$$J = 1 + \frac{a}{12b}\left[1 + \frac{a}{2b}(2b - 1)^2\right]$$

$$+ \frac{1}{480}\left(\frac{a}{b}\right)^2\left[3 + 3\left(\frac{a}{b}\right)(2b-1)^2 + \frac{1}{4}\left(\frac{a}{b}\right)^2(2b - 1)^4\right] \tag{37}$$

and by the same method but using seven terms of the Taylor's series

$$K = 1 + \frac{a}{4b}\left\{\left[\frac{3}{2}\left(\frac{a}{b}\right)(2b-1)^2\right] + 1\right\} + \frac{9}{160}\left(\frac{a}{b}\right)^2\left\{\frac{4}{3}\left[\left(\frac{a}{b}\right)(2b-1)^2\right] + 3\left(\frac{a}{b}\right)(2b-1)^2 + 1\right\} + \frac{9}{4480}\left(\frac{a}{b}\right)^3\left\{\frac{9}{8}\left[\left(\frac{a}{b}\right)(2b-1)^2\right]^3 + \frac{90}{8}\left[\frac{a}{b}(2b-1)^2\right]^2 + \frac{90}{4}\left(\frac{a}{b}\right)(2b-1)^2 + 5\right\} \quad (38)$$

Equations (37) and (38) apply for negative or positive values of b, that is, for $C_1 > C_2$ or $C_1 < C_2$ but not for $C_1 = C_2$. If $C_1 = C_2$, the expressions for J and K are

$$J = \frac{\sinh a}{a}$$

$$K = \frac{\sinh 3a}{3a}$$

These equations can easily be verified by integrating equation 1 with the curvature C constant and substituting in equations (22) and (23).

Charts of J and K/J are shown in figures 15 and 16, respectively, as a function of

$$a = \frac{C_1 n_o}{2}$$

and

$$b = \frac{-C_1}{\Delta C}$$

Evaluation of channel-surface velocities. - The relation between the velocity at the point of the center of the channel and the velocities along the surface of the channel (figs. 17 and 18) can be derived, inasmuch as from equation (21)

$$\sqrt{\frac{Z_1}{Z_m}} = \exp\left[-\frac{n_o}{2\Delta C}\left(C_1^2 - C_m^2\right)\right]$$

$$= \exp\left\{-\frac{n_o\, C_1}{2}\,\frac{C_1}{\Delta C}\left[1 - \left(\frac{C_m}{C_1}\right)^2\right]\right\}$$

$$= \exp\left[\frac{n_o\, C_1}{2}\left(1 + \frac{\Delta C}{4C_1}\right)\right]$$

$$= \exp\left[a\left(1 - \frac{1}{4b}\right)\right] \tag{39}$$

and similarly,

$$\sqrt{\frac{Z_2}{Z_m}} = \exp\left[-a\left(1 - \frac{3}{4b}\right)\right] \tag{40}$$

The velocities at the channel wall, that is, at the ends of the velocity-potential line considered, are computed from the value of Z_m by use of equations (39) and (40).

The simple stream-filament theory presented may be used to compute the velocity distribution on the surface of any channel to which the assumptions used apply.

APPENDIX B

BLADE-DESIGN PROCEDURE

The velocity distribution for cascades of high solidity may be determined by use of the stream-filament theory presented in appendix A. Blades may be drawn by inspection to fit the velocity vectors specified by the vector diagrams. Starting the blade design by first drawing the camber line seems to be practically desirable. The ends of the camber line are drawn tangent to a line at an angle of $\alpha_e + \nu_e$ from the horizontal at the trailing edge and to a line at an angle $\alpha_i + \nu_i$ at the blade entrance (fig. 19). The camber line may be symmetrically drawn about line X, vertically drawn through the camber line where its slope is zero.

A symmetrical airfoil is superimposed upon the camber line, thus a first approximation of the blade shape is formed. The maximum thickness of the symmetrical airfoil is placed at line X (fig. 20). A circle forming the leading edge is drawn with a diameter equal to about 30 percent of the maximum thickness of the foil. The trailing edge is drawn with an included angle of about 12°. The maximum thickness of the foil will, of course, depend on the total turning angle $\alpha_i + \alpha_e$ and the desired surface velocities.

An orthogonal network of streamlines and velocity-potential lines are drawn in the channel formed by two airfoils. The network may be extended ahead of and behind the cascade so that the surface velocities may be computed at any point on the blade (fig. 19). The computed surface velocities in regions from ϕ_4 to the rear stagnation point and from ϕ_8 to the front stagnation point are approximate, inasmuch as the channel is bounded by an assumed streamline in these regions. The velocities at both ends of each velocity-potential line are computed by use of the methods of appendix A.

In general, the value of $\frac{\mu n_o}{\tau}$ at the channel entrance will not be equal to that at the exit because of deviations from two-dimensional flow. For convenience, this term can be considered to vary linearly with the axial depth of the blade, as shown in figure 21. The following relations, based on the general energy equation and the isentropic relations for a perfect gas are used to evaluate $\frac{\mu n_o}{\tau}$

$$\left(\frac{\mu n_o}{\tau}\right)_i = \sqrt{\frac{\gamma-1}{\gamma+1}}\left[1 - \frac{\gamma-1}{\gamma+1}\left(\frac{V}{V_{cr}}\right)_i^2\right]^{\frac{1}{\gamma-1}}\left(\frac{V}{V_{cr}}\right)_i \cos \alpha_i \qquad (41)$$

$$\left(\frac{\mu n_o}{\tau}\right)_e = \sqrt{\frac{\gamma-1}{\gamma+1}}\left[1 - \frac{\gamma-1}{\gamma+1}\left(\frac{V}{V_{cr}}\right)_e^2\right]^{\frac{1}{\gamma-1}}\left(\frac{V}{V_{cr}}\right)_e \cos \alpha_e \qquad (42)$$

With the flow network of velocity potentials and streamlines drawn and the value of μ known for each velocity potential line, the surface velocity may be computed. The values of $\left(\frac{V}{V_{cr}}\right)_1$ and $\left(\frac{V}{V_{cr}}\right)_2$ are plotted against blade-surface length S_1 and S_2, respectively. (See fig. 22.) The velocity potential ϕ is then determined by graphically integrating the velocity-distribution profile.

$$\phi = \int V \, ds \qquad (43)$$

The velocity potential is plotted against blade-surface length S (fig. 22). Inasmuch as the absolute value of ϕ is not important, the value of ϕ_4, the velocity-potential line connecting S_1 and S_2 at the rear stagnation point on S_2, is set equal to zero on both S_1 and S_2. This plot provides a convenient method for relocating the velocity-potential lines, inasmuch as the value of S_1 and S_2 for constant values of ϕ are easily found.

The circulation Γ around the airfoil is specified by the vector diagram and is expressed as follows:

$$\begin{aligned}\Gamma &= \tau\left[(V_u)_i - (V_u)_e\right] \\ &= \tau\,(V_u)_i - \tau\,(V_u)_e \\ &= \Delta\Gamma_i - \Delta\Gamma_e\end{aligned} \qquad (44)$$

that is,

$$\Delta\Gamma_i = \tau(V_u)_i$$

$$\Delta\Gamma_e = \tau(V_u)_e$$

The difference in velocity potential on S_1 and that on S_2 at the front stagnation point is equal to $\Delta\Gamma_i$ and that at the rear stagnation point is equal to $\Delta\Gamma_e$ (fig. 22).

Inasmuch as the flow is considered irrotational, the line integral of velocity around any closed path in the flow field must equal zero.

$$\int_c V \, ds = 0 \tag{45}$$

where c, for convenience, is taken as any area in the channel bounded by two streamlines and two velocity-potential lines. For example,

$$\int_{\phi_8}^{\phi_4} V_1 \, ds_1 + \int_{\phi_4}^{\phi_8} V_2 \, ds_2 = 0 \tag{46}$$

The streamlines are so drawn that equal amounts of gas pass between them.

$$\psi = \int_o^n \rho V \, dn = n_o \int_o^{\frac{n}{n_o}} \rho V \, d\left(\frac{n}{n_o}\right) \tag{47}$$

The value of $\left(\frac{n}{n_o}\right)_i$ for ψ_i ($i = 1, 2, 3, \ldots j$; where there are j streamlines) is graphically found by plotting ρV against $\frac{n}{n_o}$ (fig. 23) and integrating graphically (fig. 24).

Then,

$$\psi_i = \frac{i-1}{j-1} W \tag{48}$$

that is,

$$\psi_1 = 0, \psi_2 = \frac{W}{4}, \psi_3 = \frac{2}{4} W \quad \text{for} \quad j = 5$$

These relations are used to relocate the potential lines and the streamlines. The velocities are recomputed and the flow network again checked. Satisfactory accuracy is usually obtained in two adjustments of the flow network.

The accuracy of the network from ϕ_4 and the rear stagnation point and from ϕ_8 and the front stagnation point cannot be checked, inasmuch as the accuracy of the assumed streamline bounding the channel in these regions cannot be checked by these methods. If the network for uniform flow some distance ahead of and behind the cascade is, however, smoothly blended with the network between the blade surfaces, the surface velocities from ϕ_4 to the rear stagnation point and from ϕ_8 to the front stagnation point can be approximated with reasonable accuracy.

The first approximation of the blade shape may be altered by increasing the camber or changing the blade thickness or otherwise altering the blade shape to satisfy equation (44) and to establish a desirable velocity distribution. For example, it is desirable to have the maximum velocity on the blade surface no more than 15 percent greater than the leaving velocity, as specified by the vector diagram, inasmuch as too great a reduction in velocity in the region of the trailing edge on the suction surface is likely to result in flow separation. Accelerating flow over as much of the blade surface as possible in order to minimize boundary-layer growth is also desirable.

Blade sections are developed for a number of radii and faired to form a complete blade. Stator blades may be designed with a linear taper, but the operating stress in a rotor blade for a given tip speed will be reduced if a parabolic taper is used.

REFERENCES

1. Lighthill, M. J.: A Mathematical Method of Cascade Design. R. & M. No. 2104, British A.R.C., 1945.

2. Weinig, F.: The Flow around Turbine and Compressor Blades. CGD 291, reproduced by Code 338, Res. and Standards Branch, BuShips, Navy Dept., May 1946. (Abs. Bib. Sci. Ind. Res., vol. 2, no. 13, April 5, 1946, p. 997, PB 28689.)

3. Goldstein, Arthur W., and Jerrison, Meyer: Isolated and Grid Airfoils with Prescribed Velocity Distribution. NACA TN No. 1308, 1947.

4. Katzoff, S., Finn, Robert S., and Laurence, James C.: Interference Method for Obtaining the Potential Flow past an Arbitrary Cascade of Airfoils. NACA TN No. 1252, 1947.

5. Stodola, A.: Steam and Gas Turbines. Vol. II. McGraw-Hill Book Co., Inc., 1927, p. 992. (Reprinted, Peter Smith (New York), 1945.)

6. Goldstein, Arthur W.: Analysis of the Performance of a Jet Engine from Characteristics of the Components. I - Aerodynamics and Matching Characteristics of the Turbine Component Determined with Cold Air. NACA TN No. 1459, 1947.

7. Jahnke, Eugen, and Emde, Fritz: Table of Functions. Dover Pub. (New York), 4th ed., 1945, p. 32.

TABLE I - BLADE COORDINATES

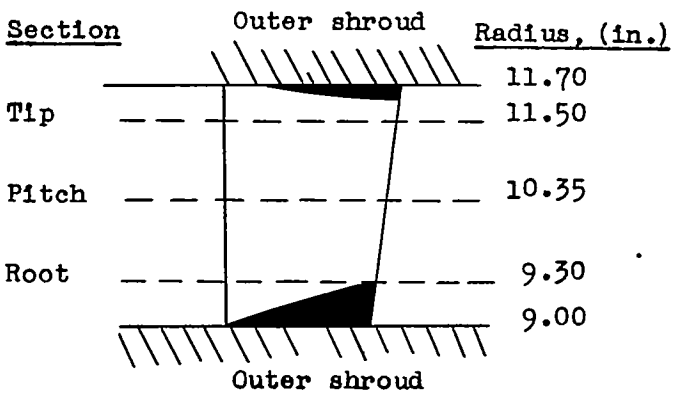

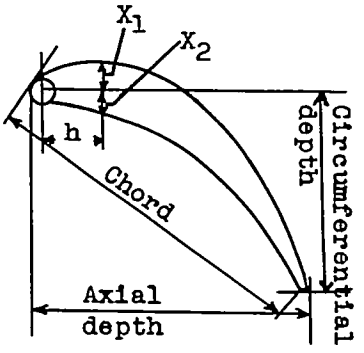

Shaded areas are boundary layer

	Root section		Pitch section		Tip section	
h (in.)	X_1 (in.)	X_2 (in.)	X_1 (in.)	X_2 (in.)	X_1 (in.)	X_2 (in.)
0	0.063	-0.053	0.063	-0.053	0.063	-0.053
.100	.114	- .068	.114	- .068	.114	- .068
.200	.148	- .083	.148	- .083	.148	- .083
.300	.168	- .110	.167	- .105	.165	- .100
.400	.179	- .138	.173	- .130	.167	- .122
.500	.172	- .171	.164	- .161	.156	- .151
.600	.152	- .211	.143	- .199	.134	- .187
.700	.117	- .258	.107	- .234	.096	- .229
.800	.064	- .316	.053	- .299	.041	- .281
.900	- .012	- .388	- .016	- .365	- .029	- .342
1.000	- .116	- .471	- .115	- .442	- .114	- .412
1.100	- .245	- .569	- .229	- .531	- .212	- .493
1.200	- .407	- .686	- .369	- .638	- .331	- .589
1.300	- .612	- .835	- .542	- .769	- .471	- .703
1.400	- .869	-1.022	- .754	- .930	- .638	- .838
1.500	-1.176	-1.244	-1.008	-1.126	- .840	-1.001
1.600					-1.101	-1.178

Section	Pitch (in.)	Chord (in.)	Axial depth (in.)	Circumferential depth (in.)	Leading-edge radius (in.)	Trailing-edge radius (in.)
Root	1.193	2.052	1.535	1.275	0.050	0.010
Mean	1.334	2.074	1.585	1.245	.050	.010
Tip	1.475	2.100	1.638	1.216	.050	.010

TABLE II - POSITION OF BLADE PRESSURE TAPS

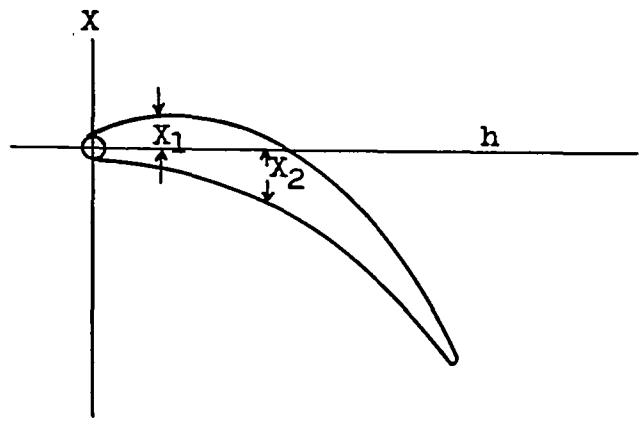

Root section			Pitch section			Tip section		
h (in.)	X_1 (in.)	X_2 (in.)	h (in.)	X_1 (in.)	X_2 (in.)	h (in.)	X_1 (in.)	X_2 (in.)
-0.050	0	0	-0.050	0	0	-0.050	0	0
.200	.150		.200	.149		.200	.148	
.400	.178		.400	.173		.400	.168	
.700	.119		.700	.108		.700	.097	
1.000	-.114		1.000	-.115		1.000	-.114	
1.300	-.614		1.300	-.543		1.300	-.472	
1.435	-.970		1.435	-.934		1.435	-.890	
1.300		-.835	1.300		-.770	1.300		-.706
1.100		-.570	1.100		-.532	1.100		-.497
.800		-.316	.800		-.299	.800		-.281
.500		-.172	.500		-.162	.500		-.152
.300		-.110	.300		-.105	.300		-.100

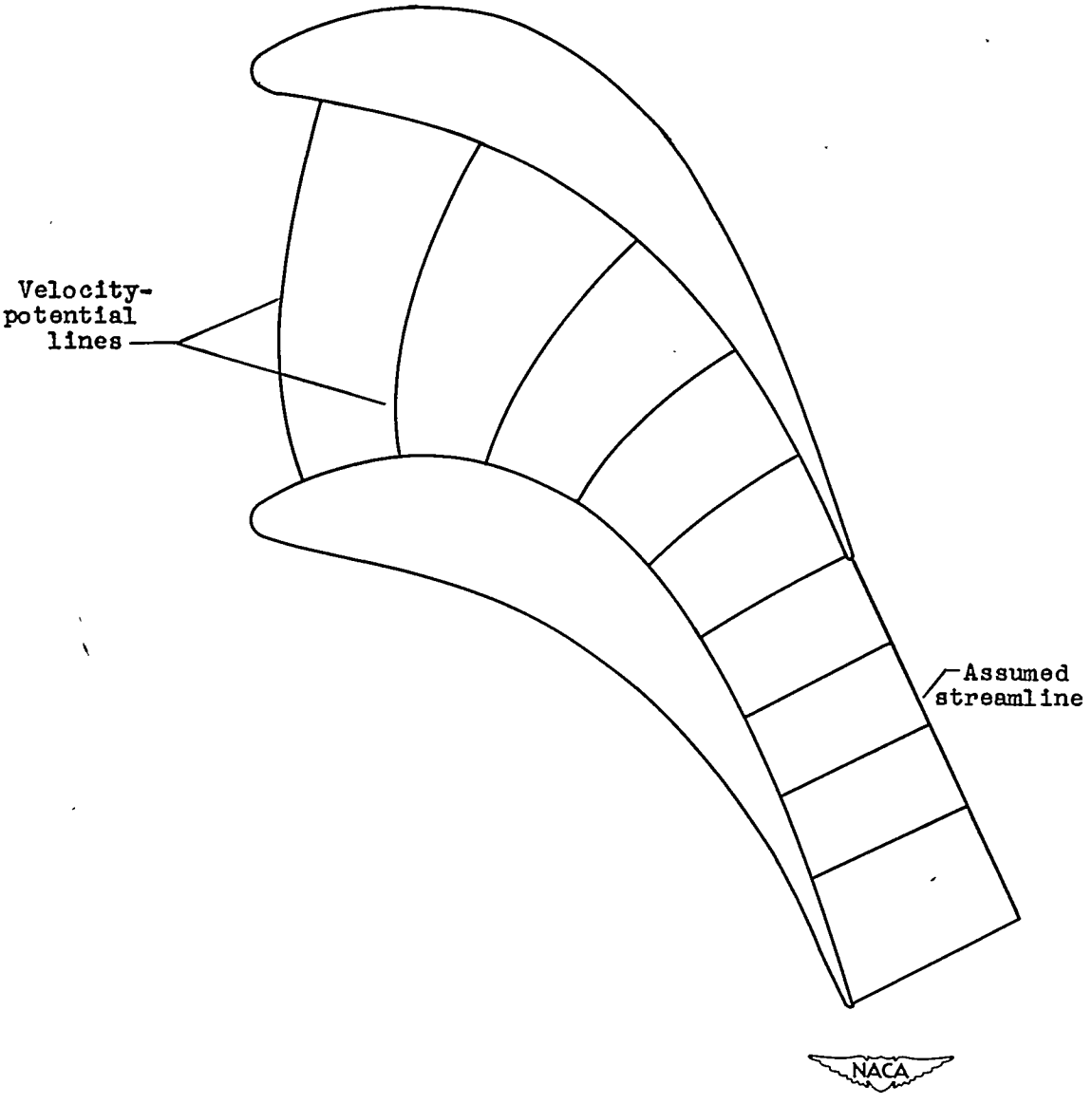

Figure 1.- Blade section showing potential lines used for calculating the surface velocities.

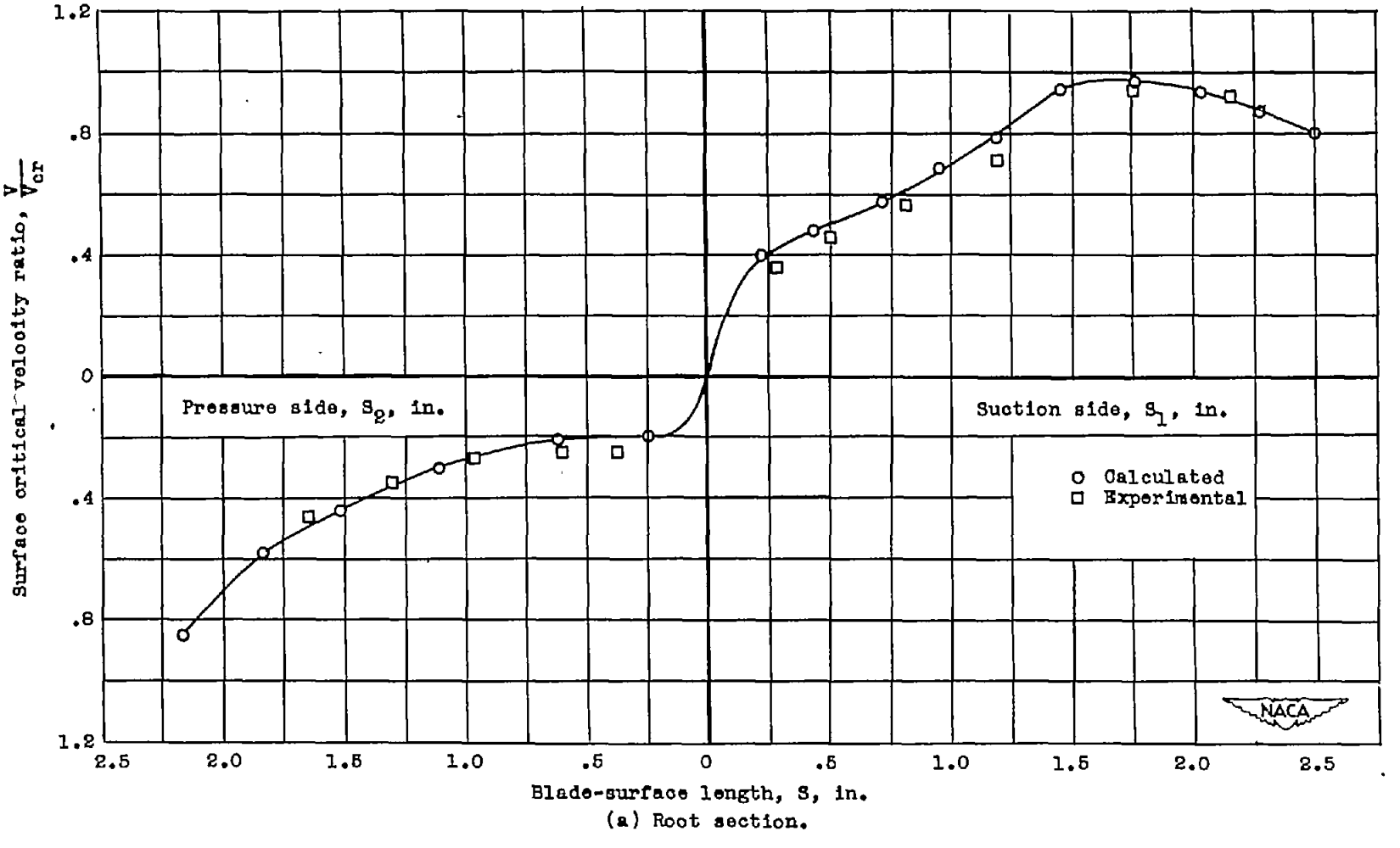

(a) Root section.

Figure 2.- Blade-surface velocities at design conditions.

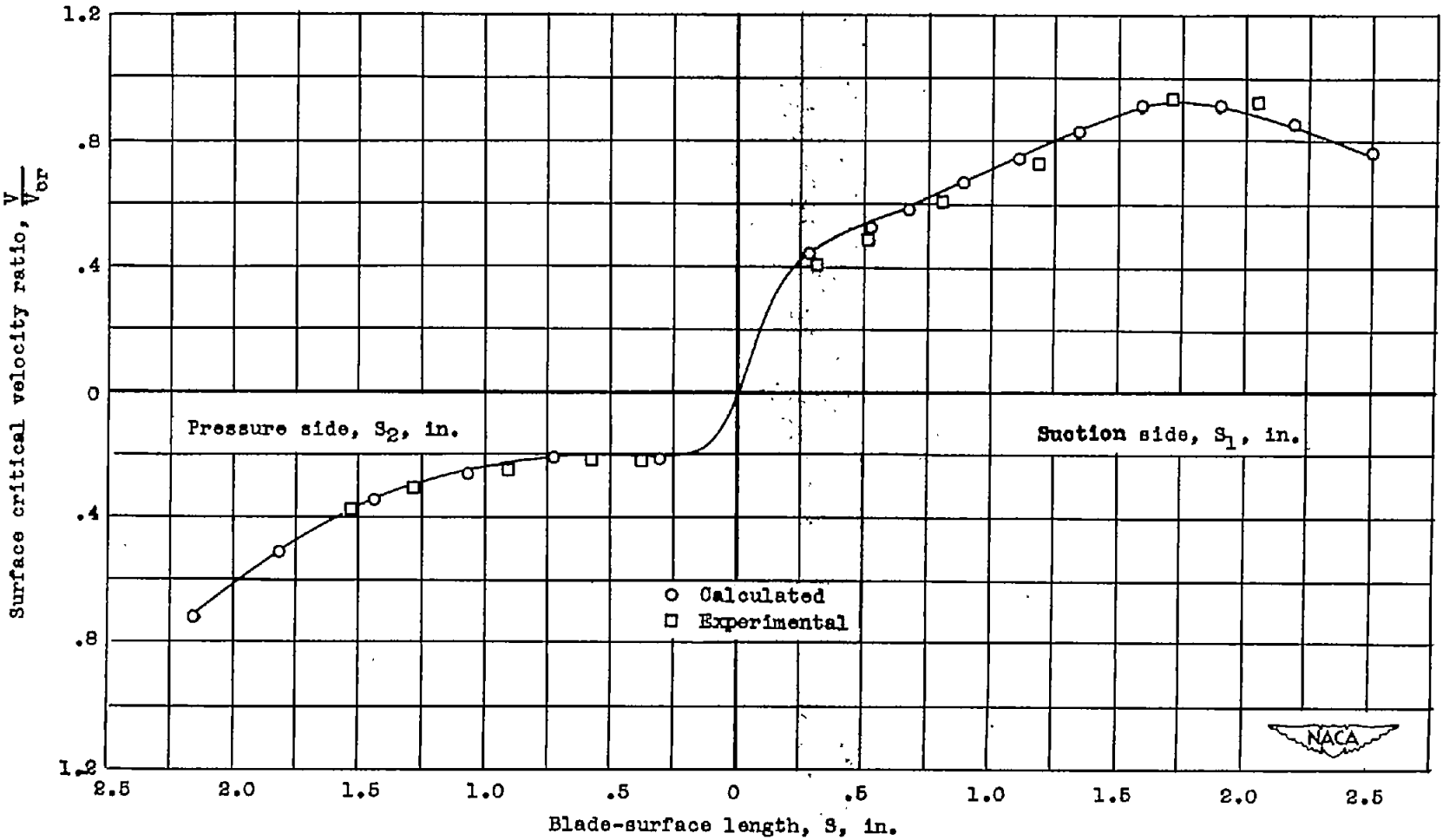

(b) Pitch section.

Figure 2.- Continued. Blade-surface velocities at design conditions.

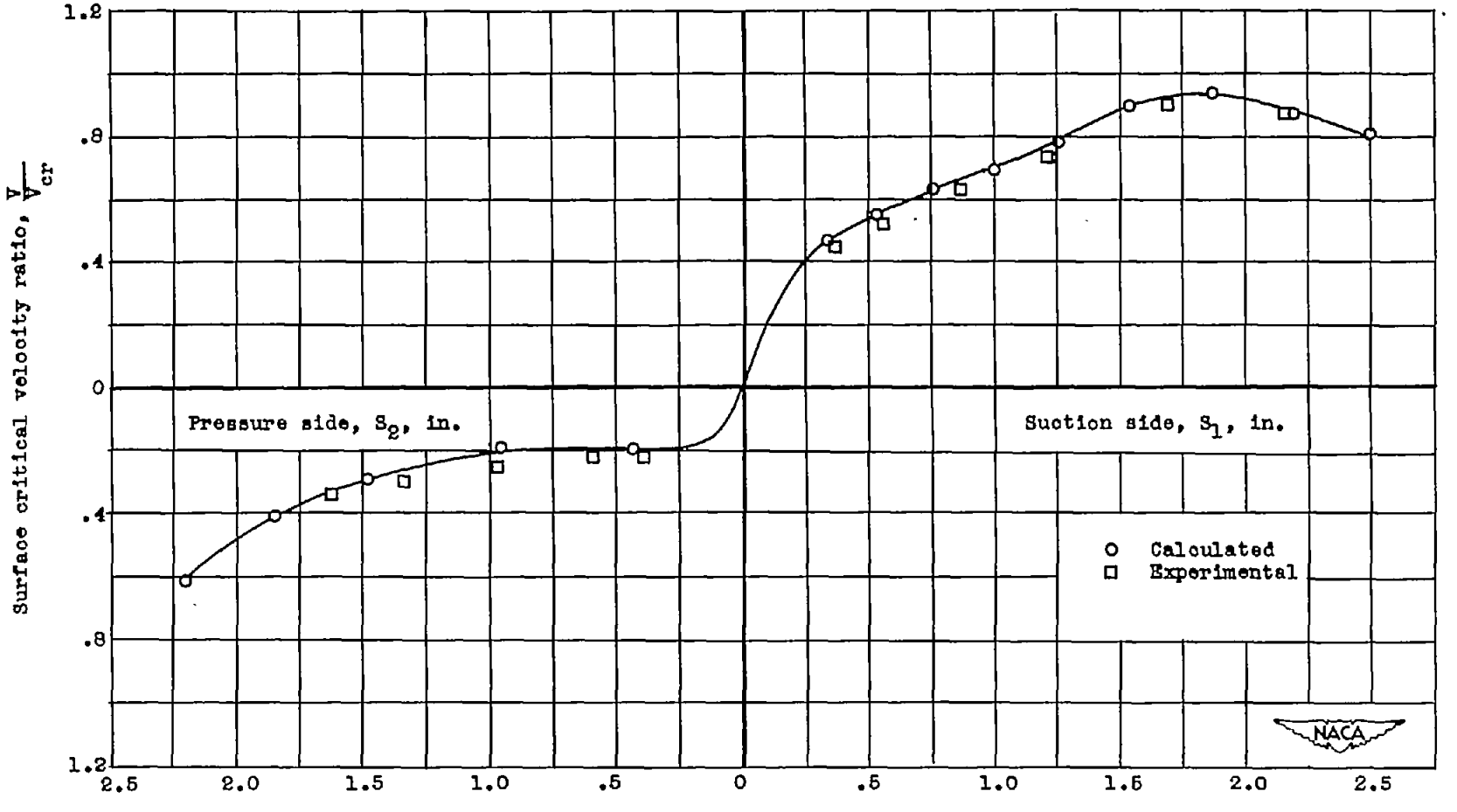

Blade-surface length, S, in.

(c) Tip section.

Figure 2.- Concluded. Blade-surface velocities at design conditions.

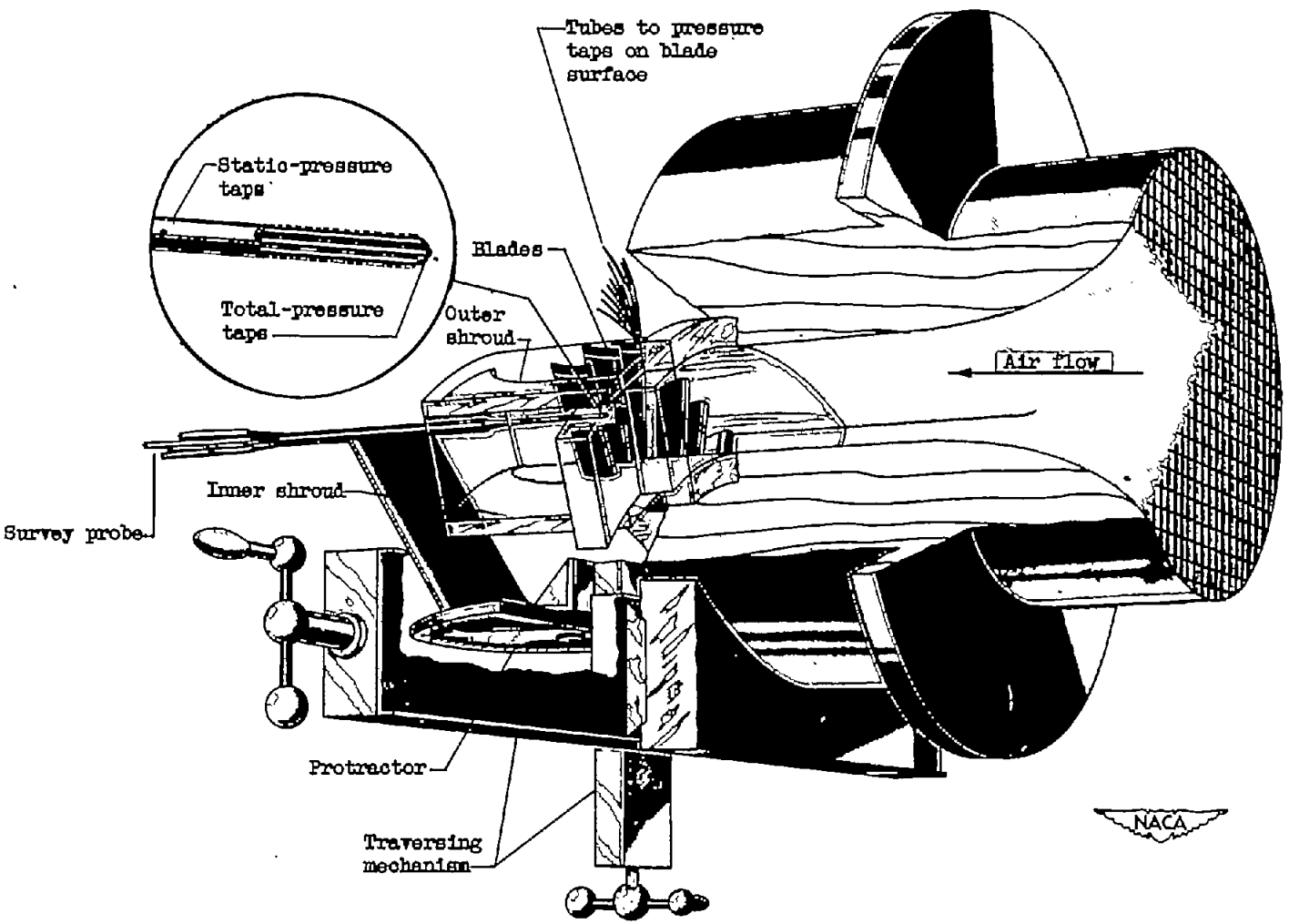

Figure 3.- Turbine-blade-cascade experimental equipment.

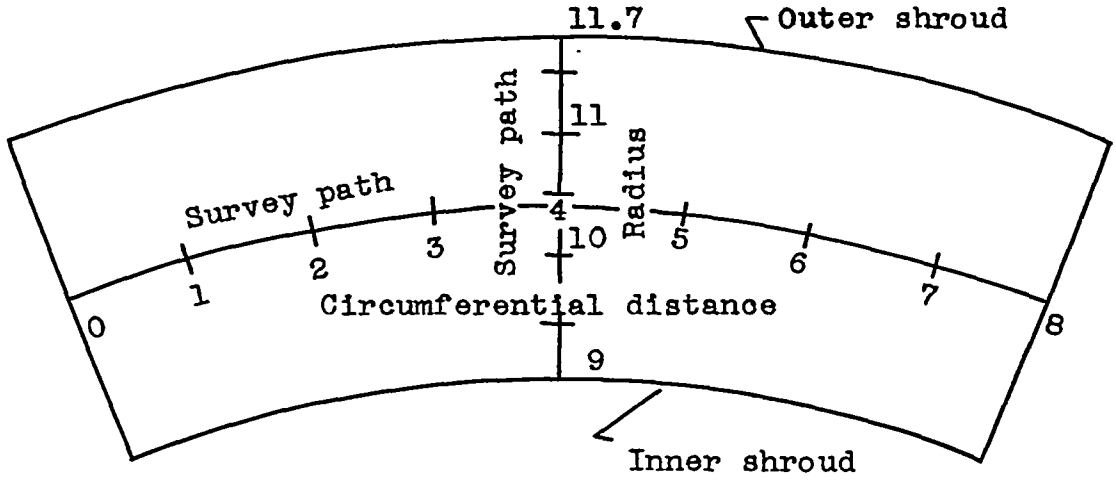

Figure 4.- Survey planes 1.5 chord lengths upstream of the turbine blades. (All dimensions are given in inches.)

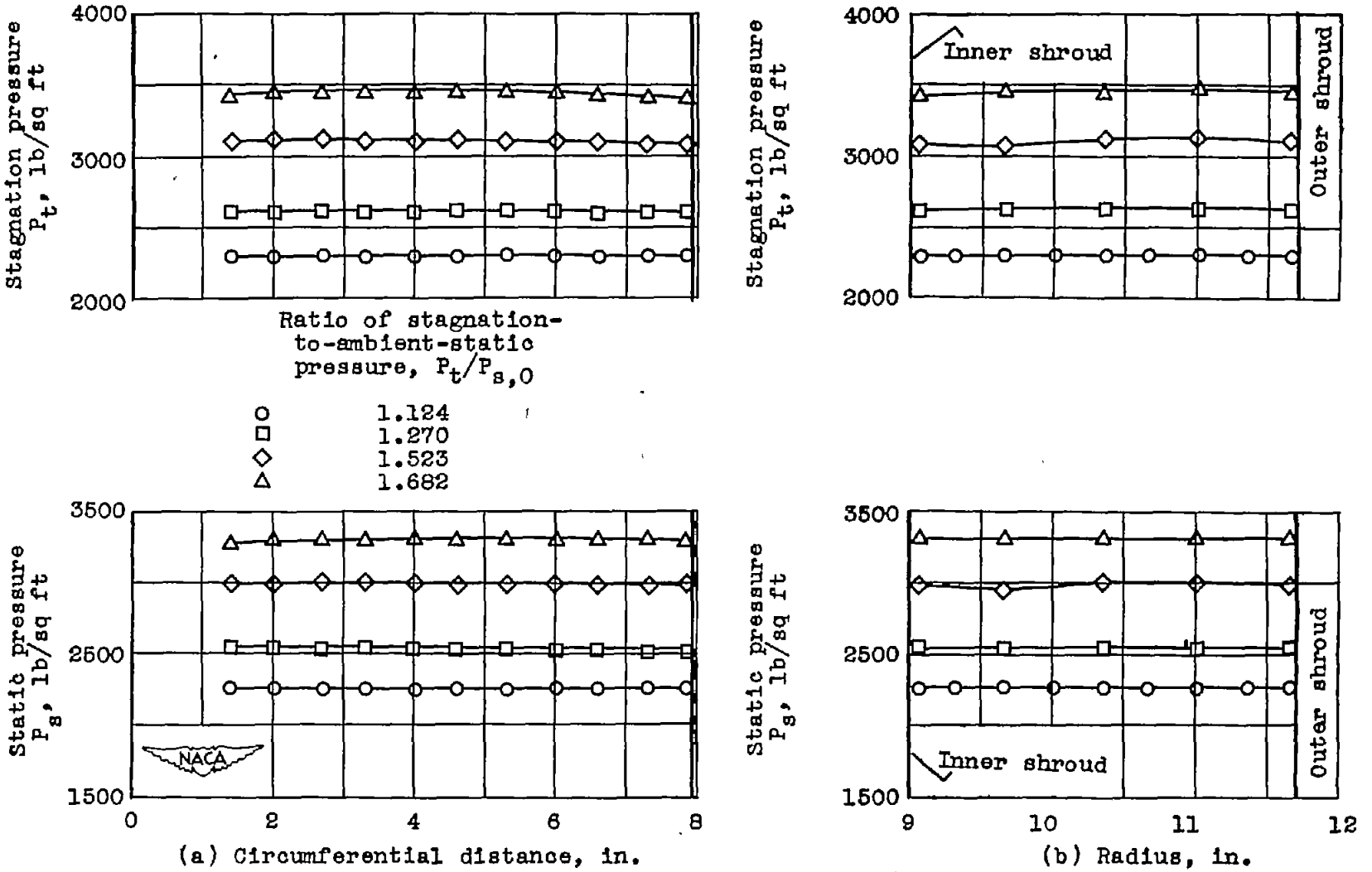

Figure 5. - Variation of stagnation and static pressures in the cascade tunnel at 1.5 chord lengths upstream of the turbine blades.

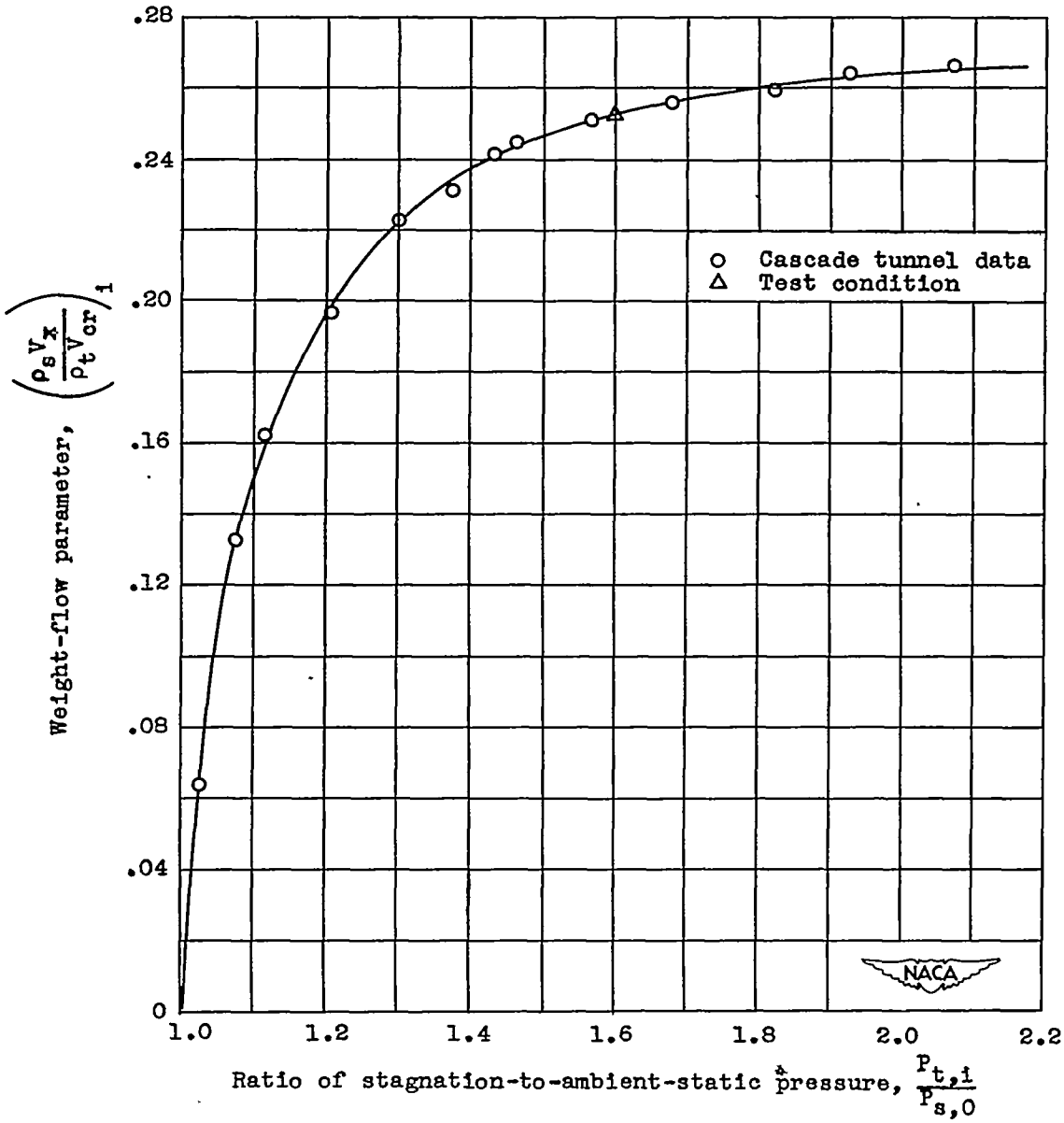

Figure 6. - Variation of weight-flow parameter at cascade entrance with ratio of stagnation-to-ambient-static pressure across cascade.

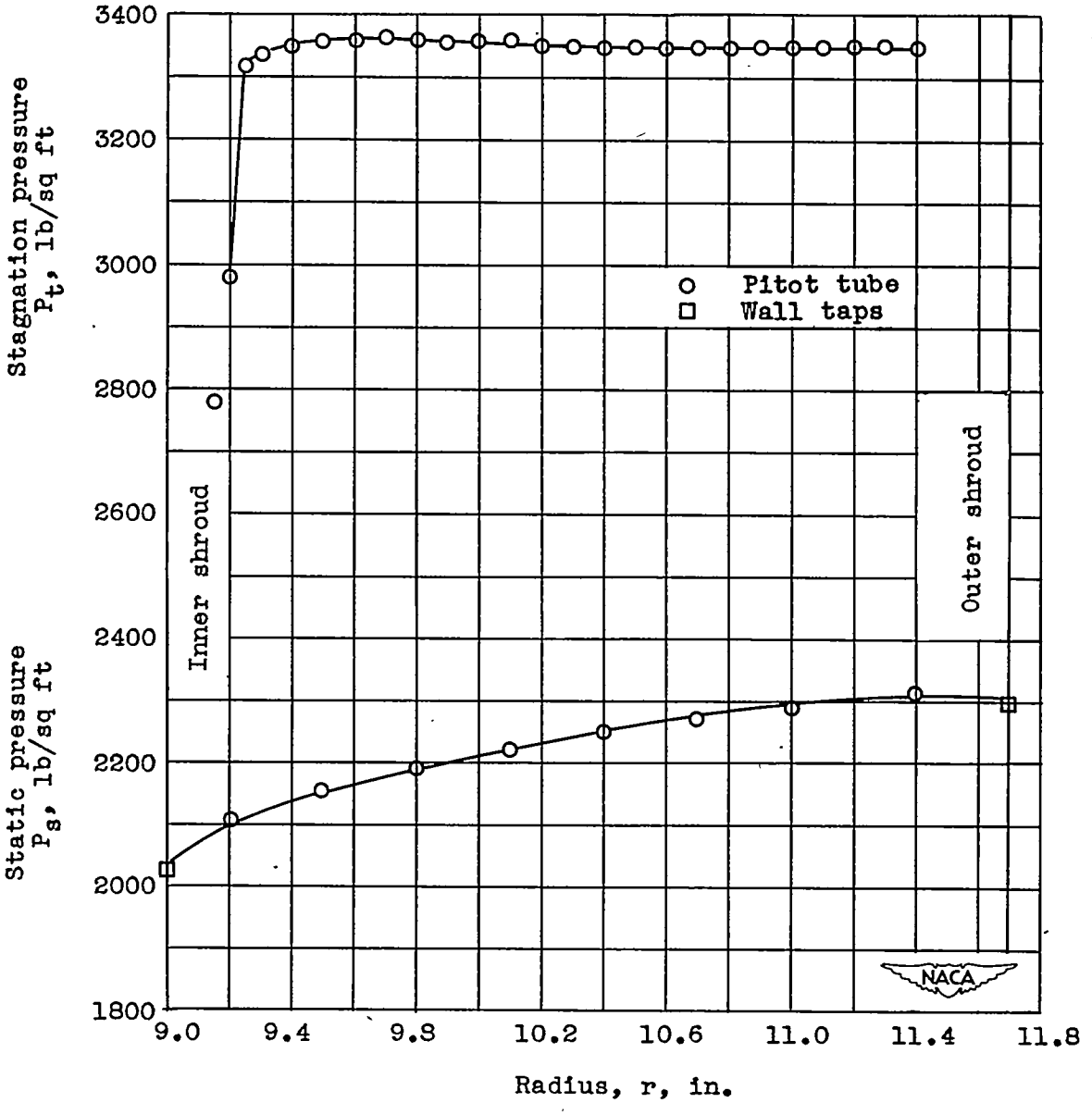

Figure 7. - Measured stagnation and static pressure at 0.1 chord downstream of cascade.

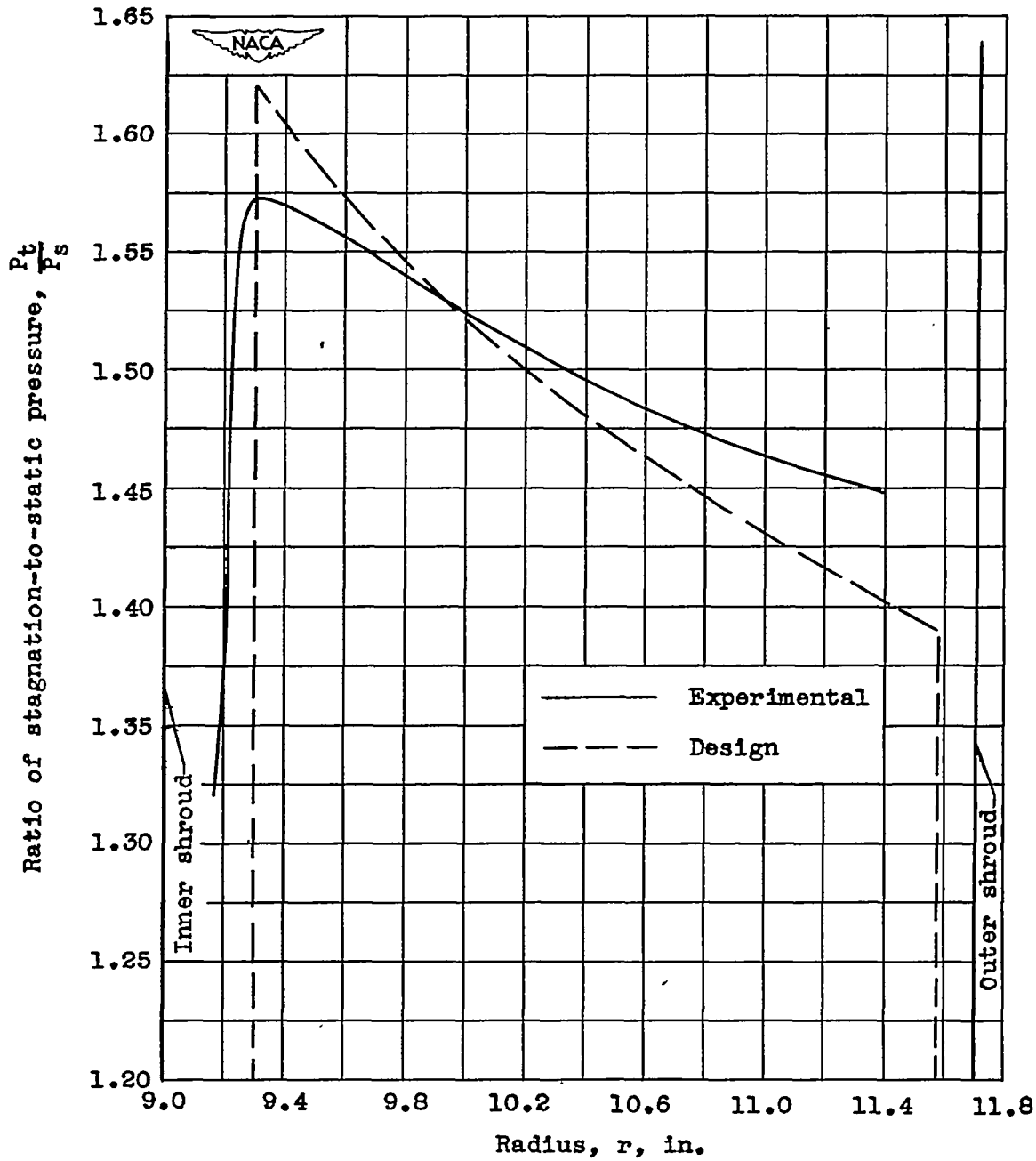

Figure 8. - Comparison of ratios of experimental and design stagnation-to-static pressure at 0.1 chord downstream of blades.

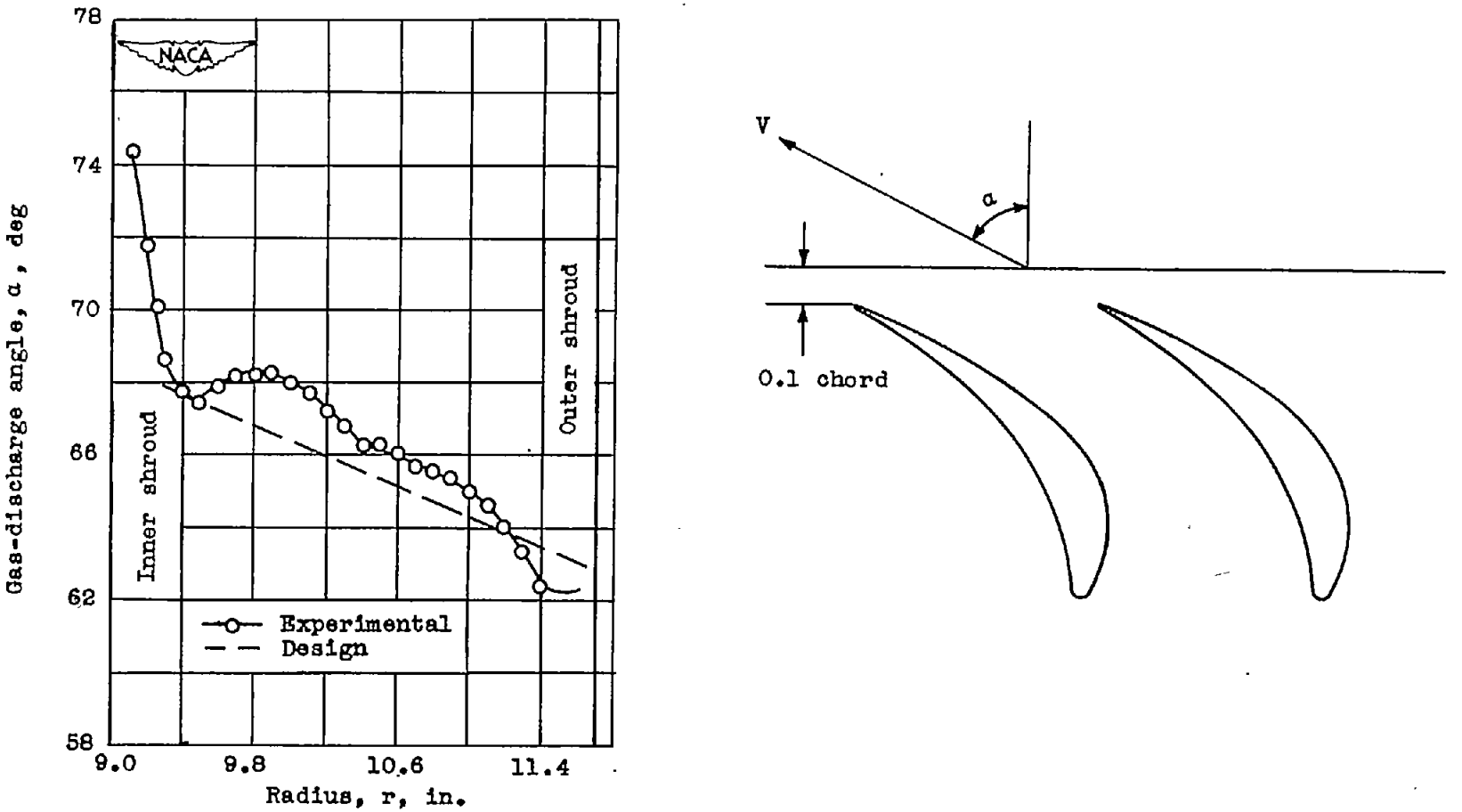

(a) Radial variation.

Figure 9. - Variation of gas-discharge angle at 0.1 chord downstream of cascade.

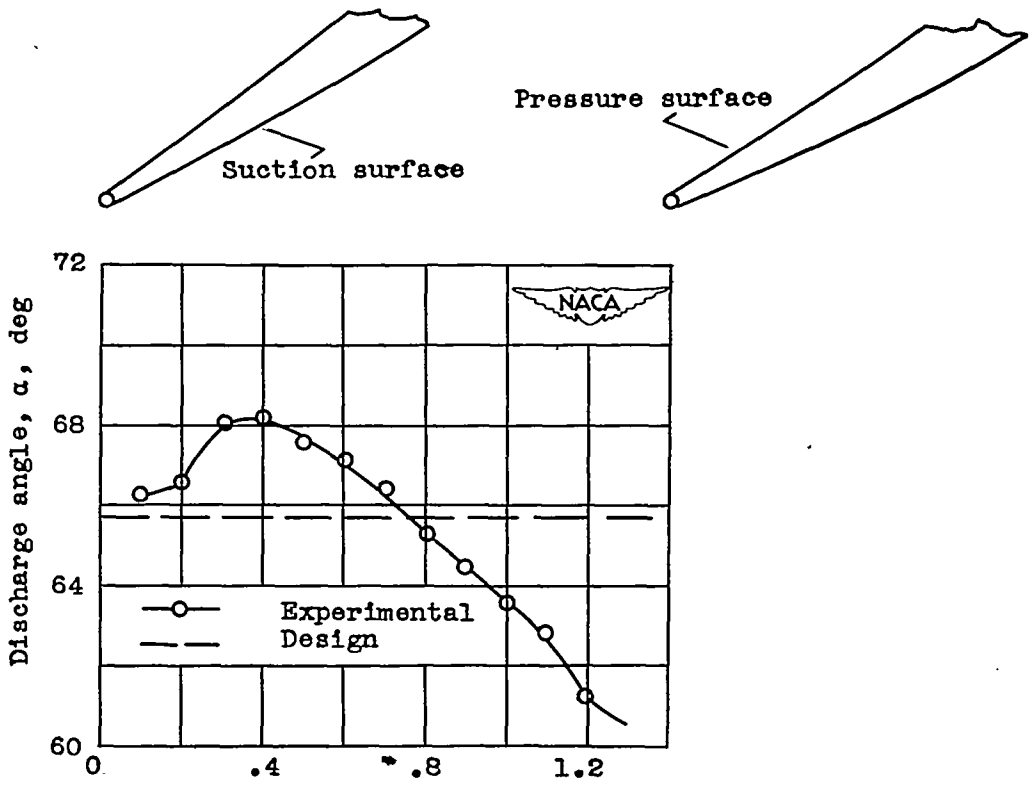

(b) Circumferential variation at the 10.35-in. radius.

Figure 9.- Concluded. Variation of discharge angle at 0.1 chord downstream of cascade.

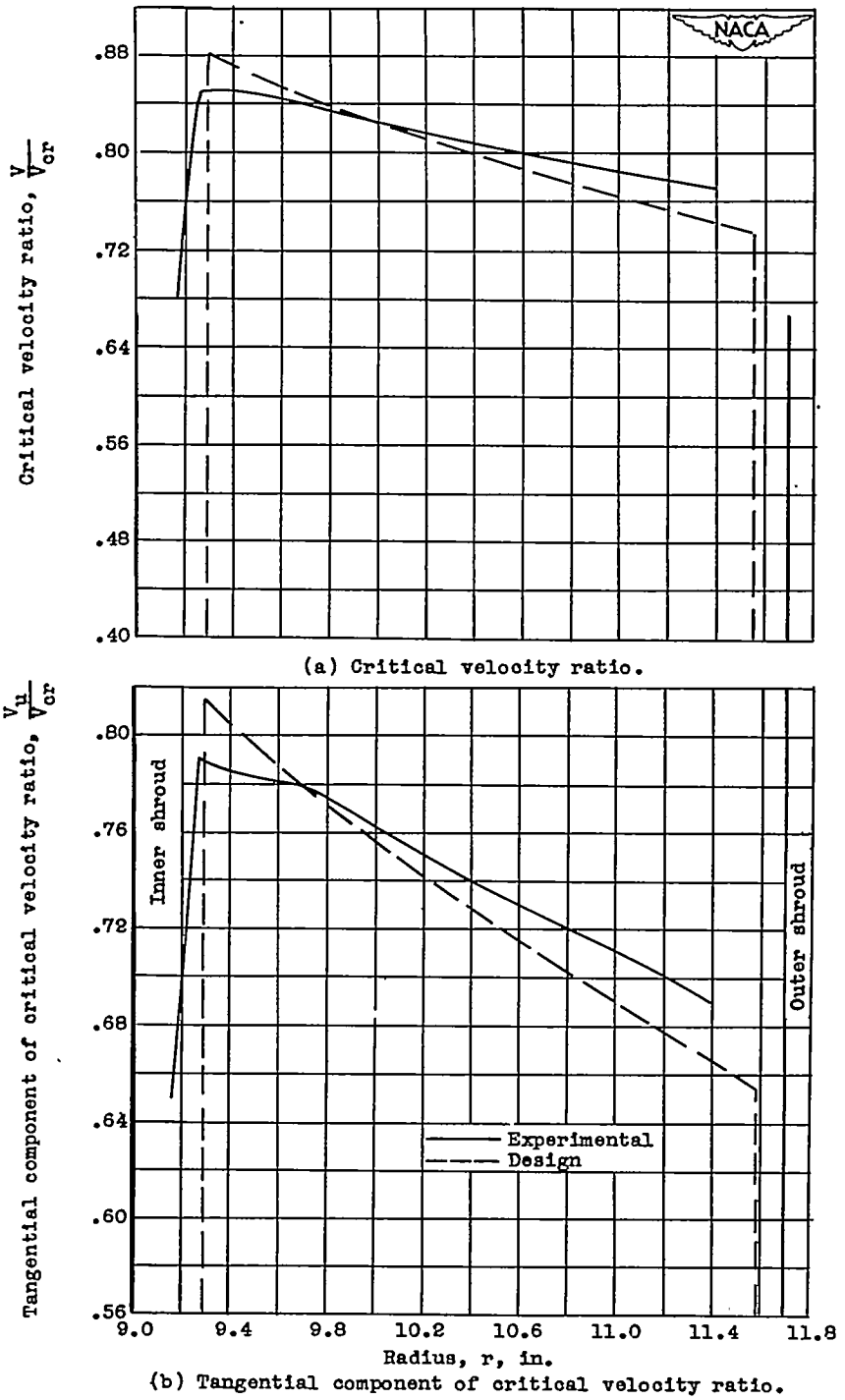

(a) Critical velocity ratio.

(b) Tangential component of critical velocity ratio.

Figure 10.- Radial variation of critical ratio $\frac{V}{V_{cr}}$ and tangential component of critical velocity ratio $\frac{V_u}{V_{cr}}$ at 0.1 chord downstream of cascade.

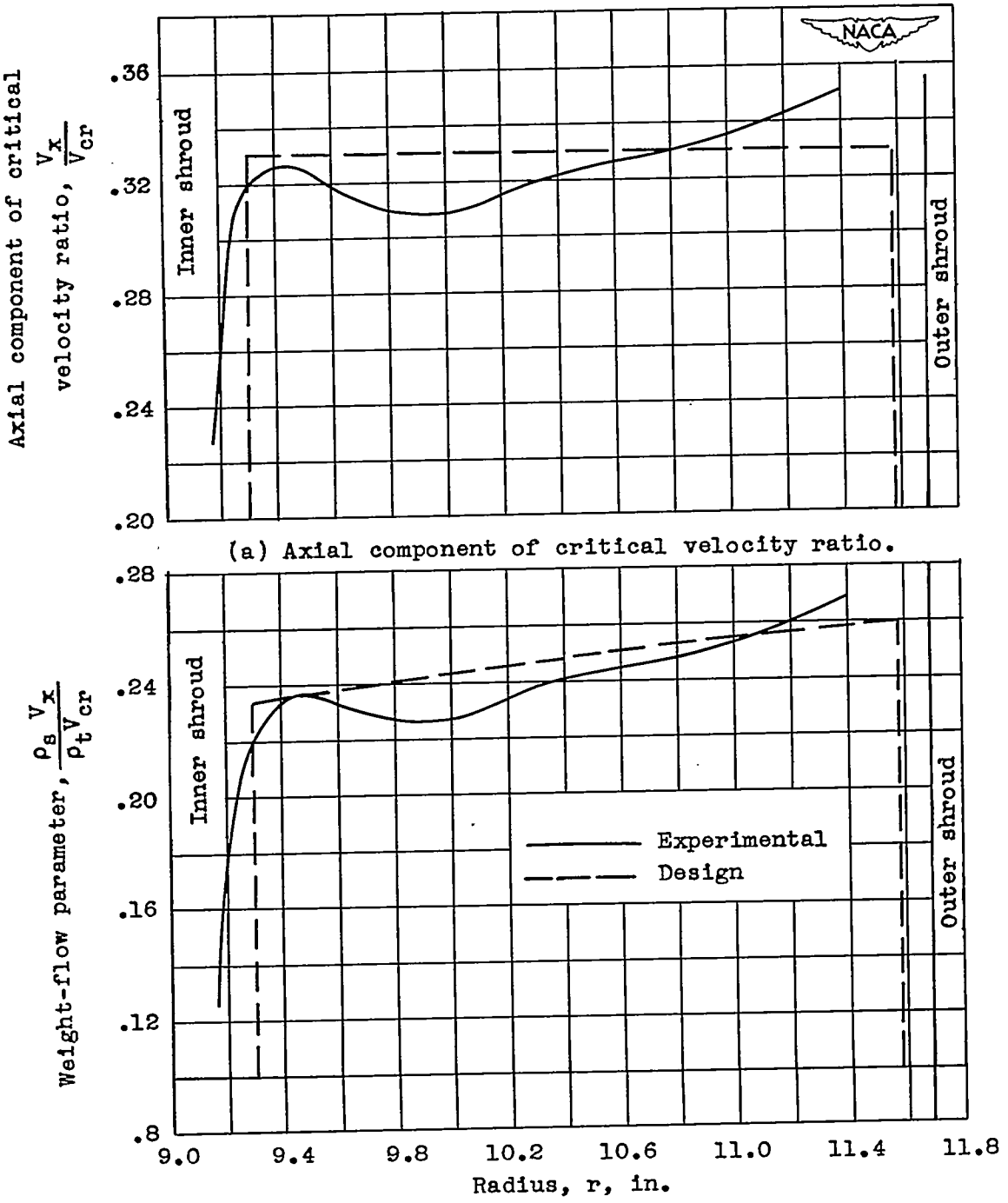

(a) Axial component of critical velocity ratio.

(b) Weight-flow parameter.

Figure 11.- Radial variation of axial component of velocity $\frac{V_x}{V_{cr}}$ and weight-flow parameter at 0.1 chord downstream of cascade.

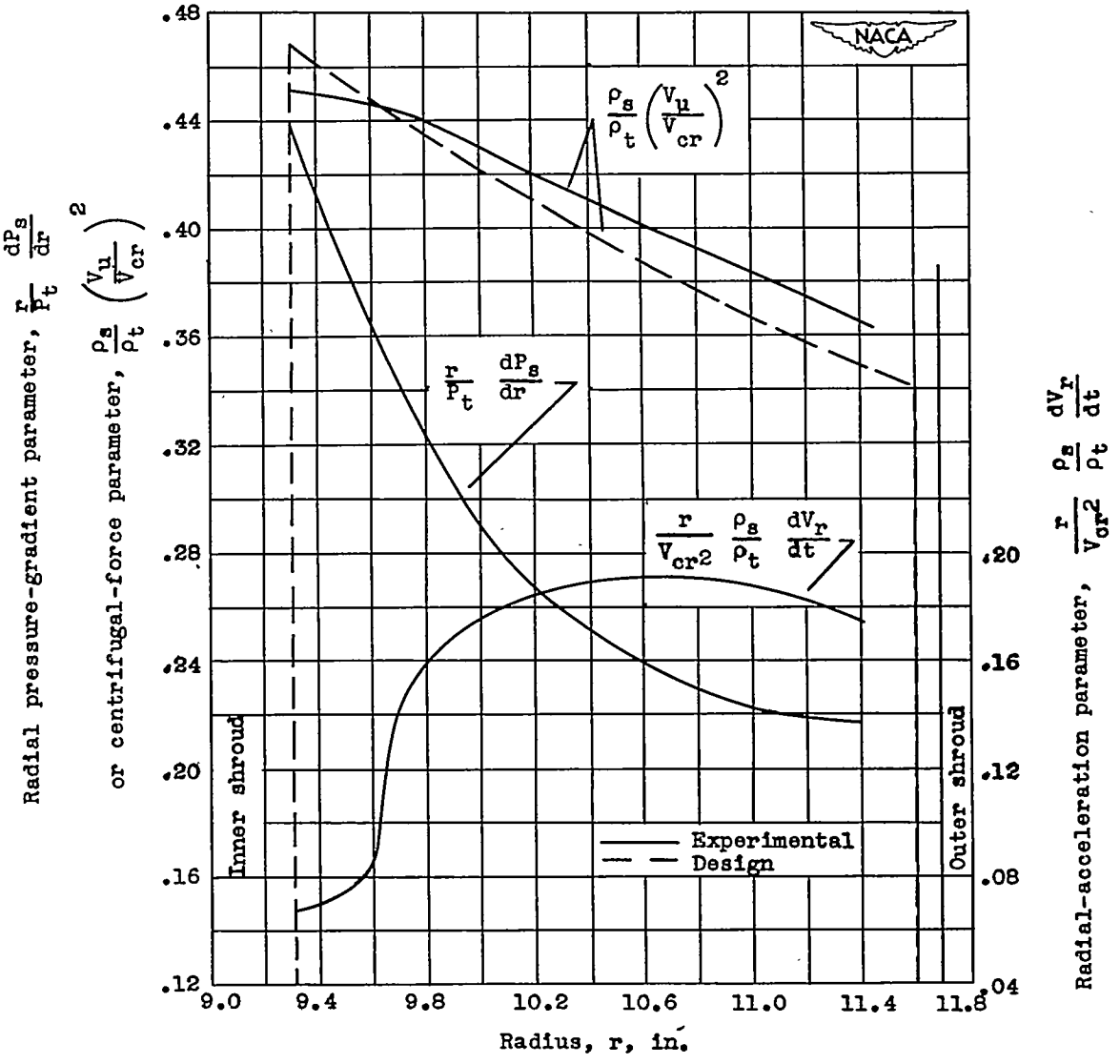

Figure 12.- Radial equilibrium parameters.

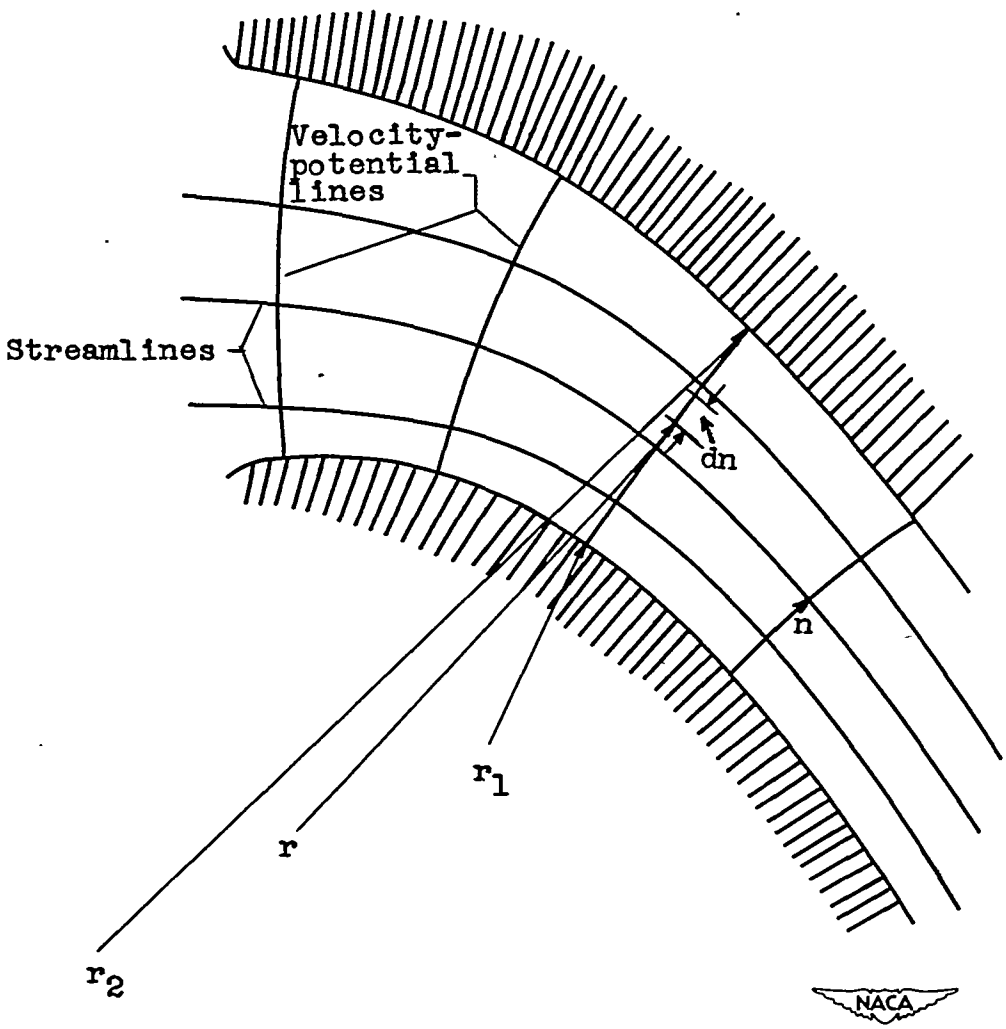

Figure 13.- The flow of a gas in the channel between curved surfaces.

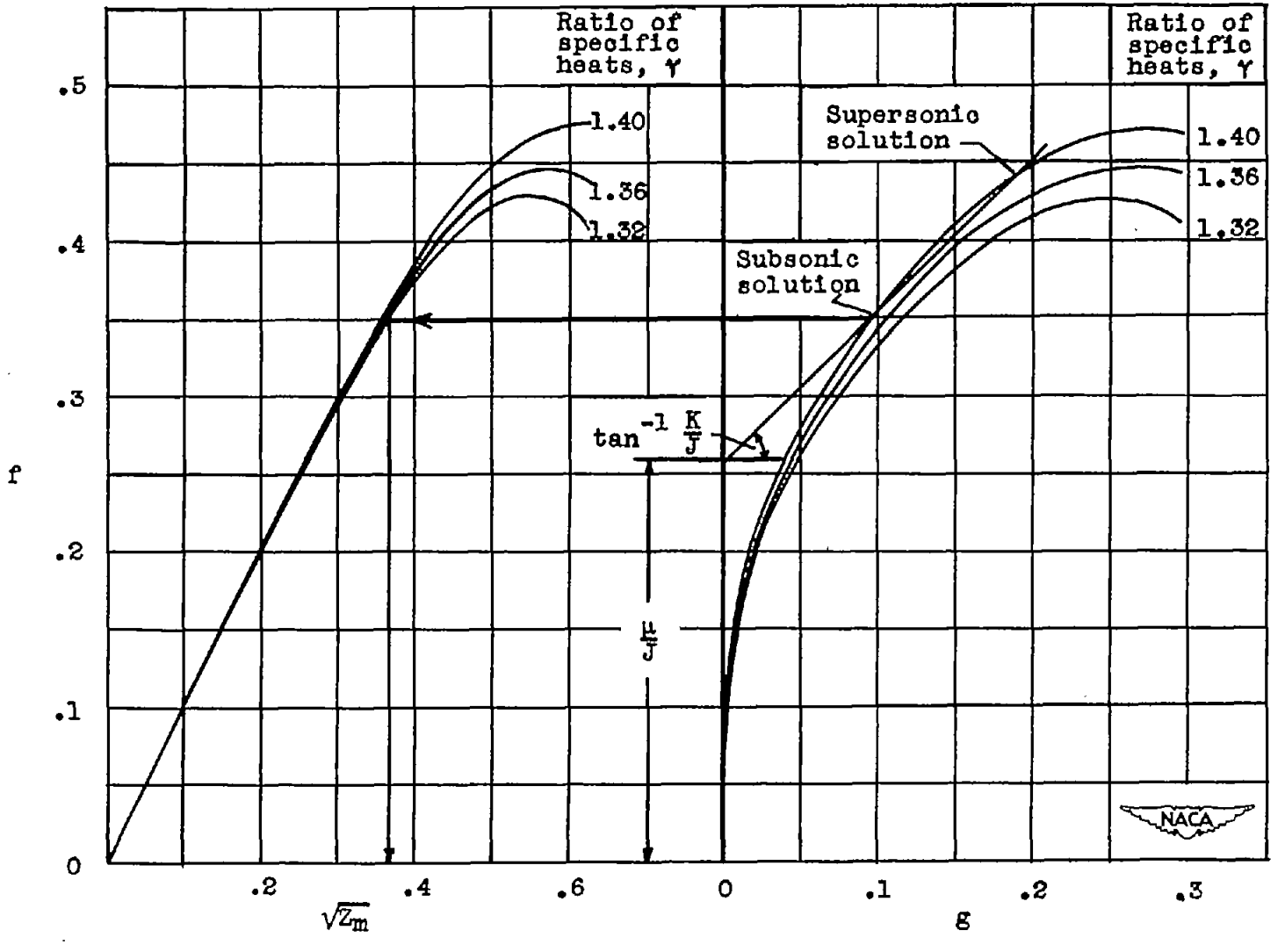

Figure 14.- Chart for finding the average velocity through the blade channel.
(Two 12-by-20-in. prints of this figure are attached.)

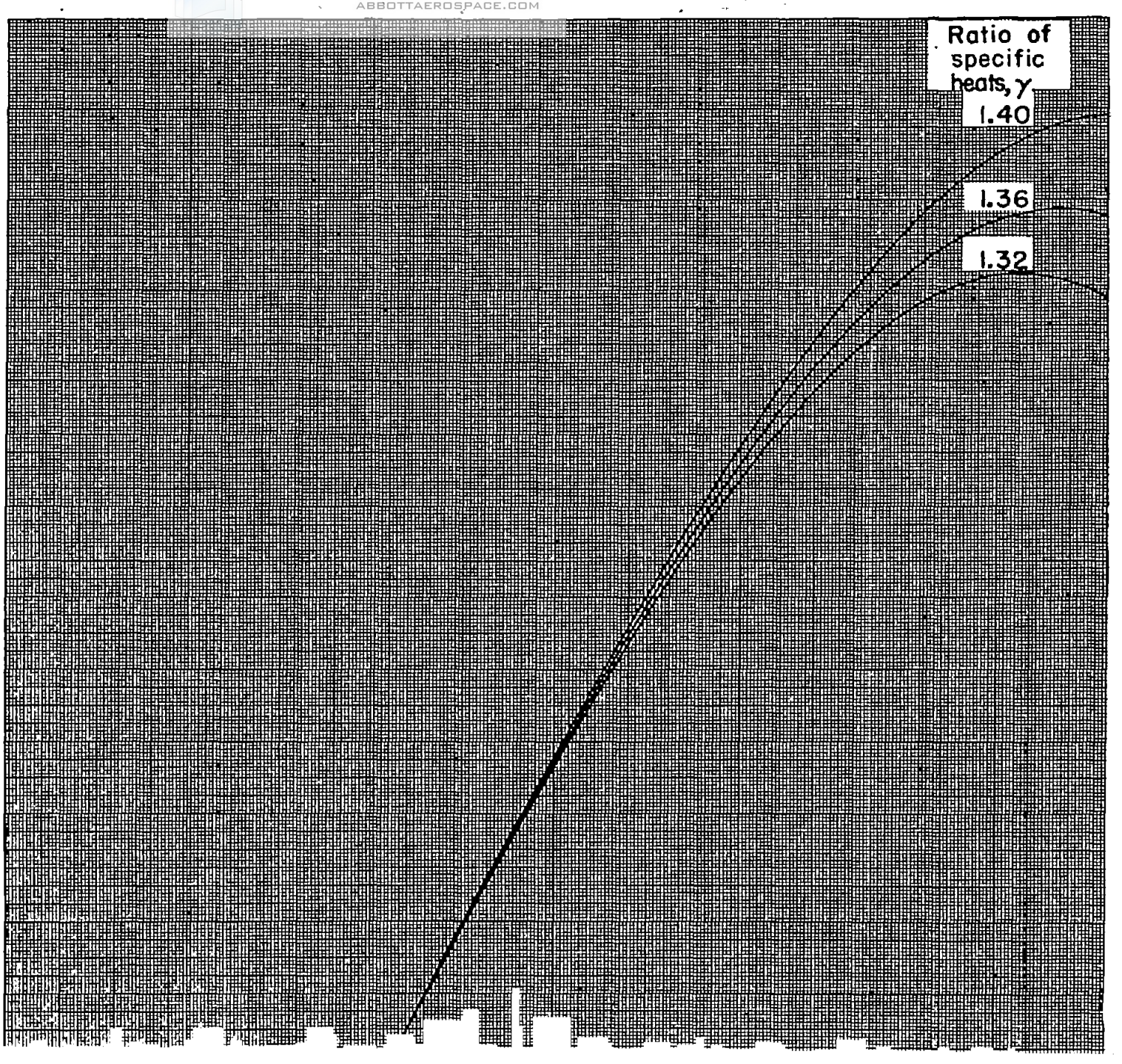

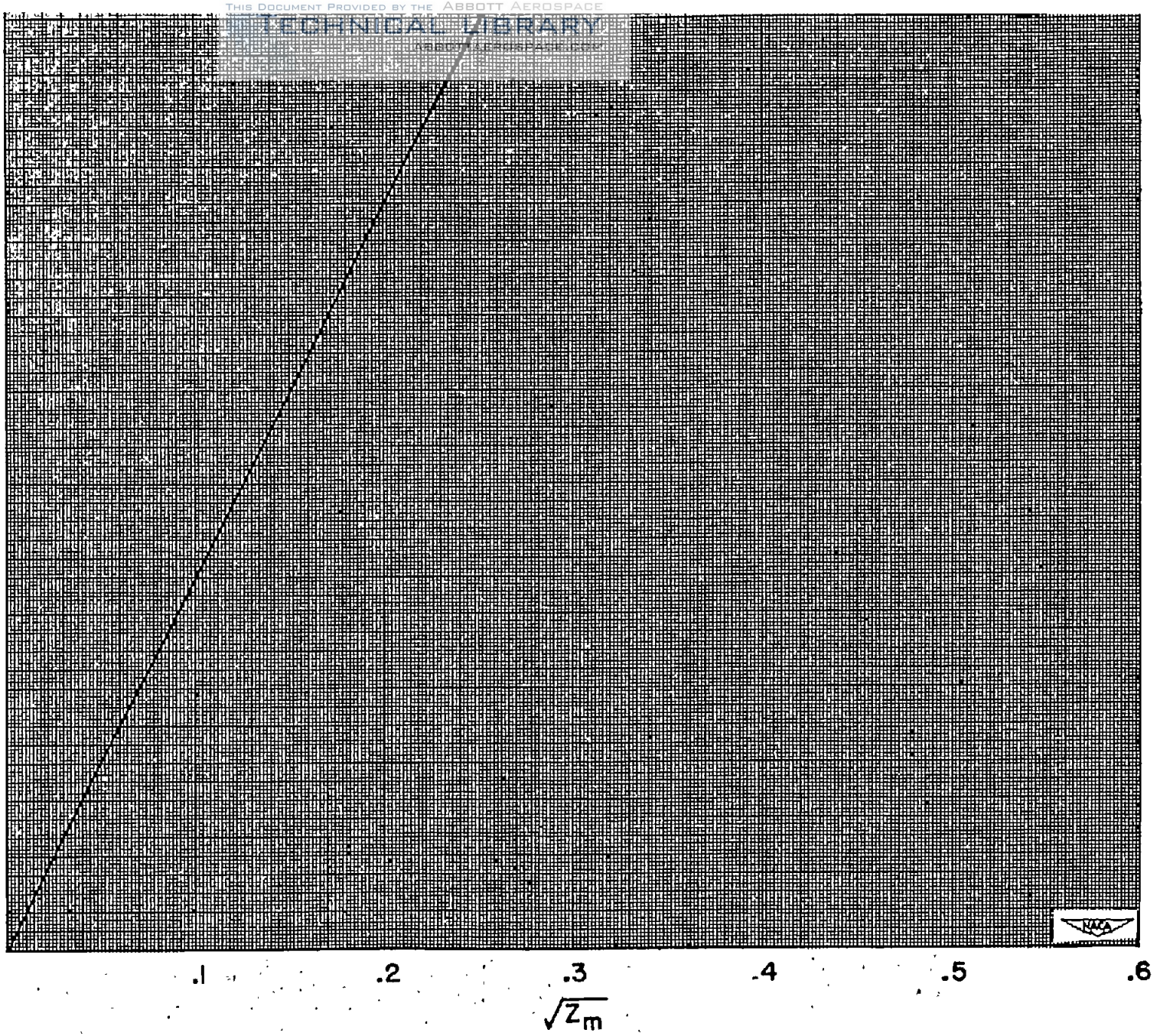

(a) Chart for finding $\sqrt{Z_m}$.

Figure 14. - Chart for finding average velocity through blade channel.

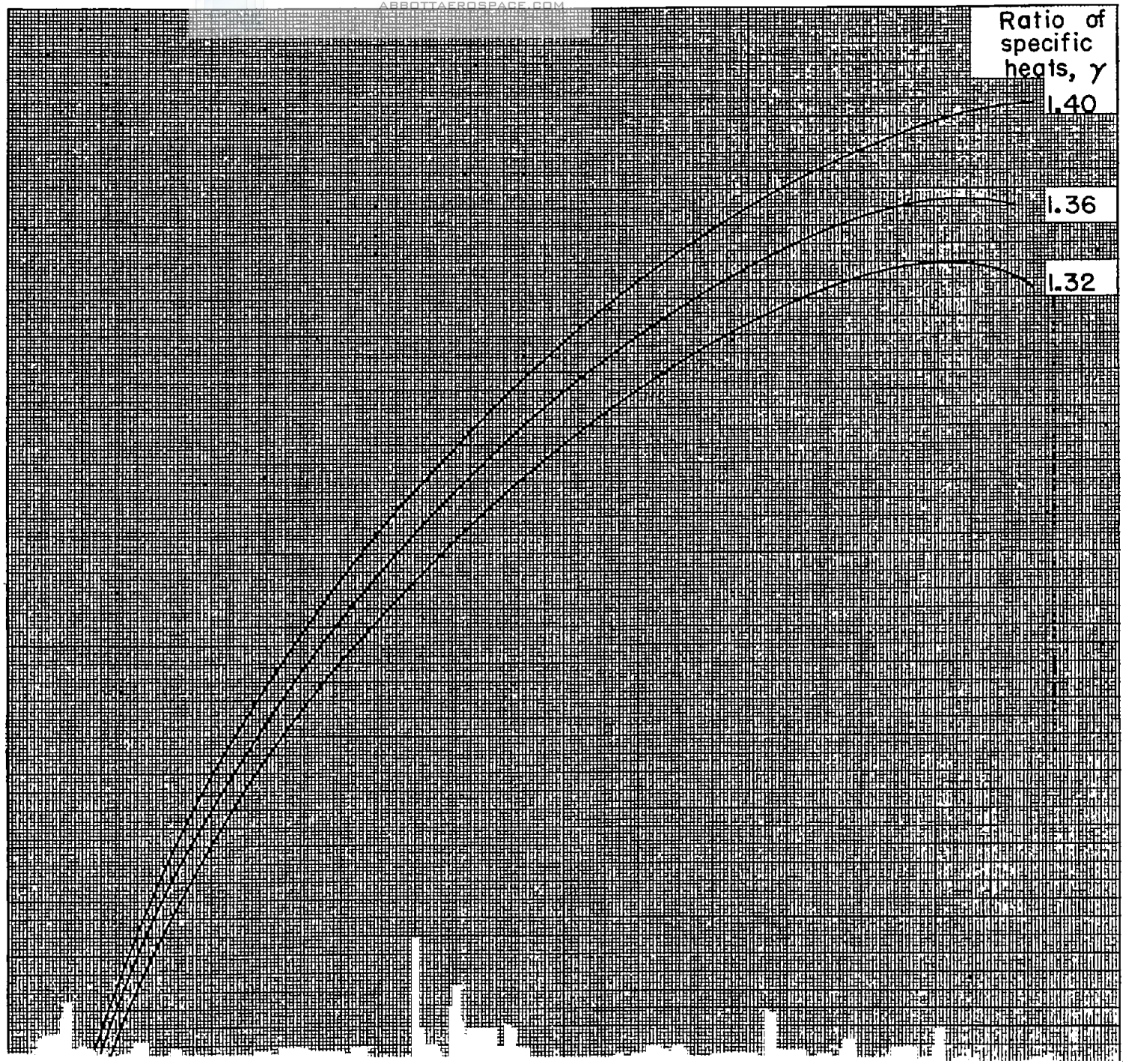

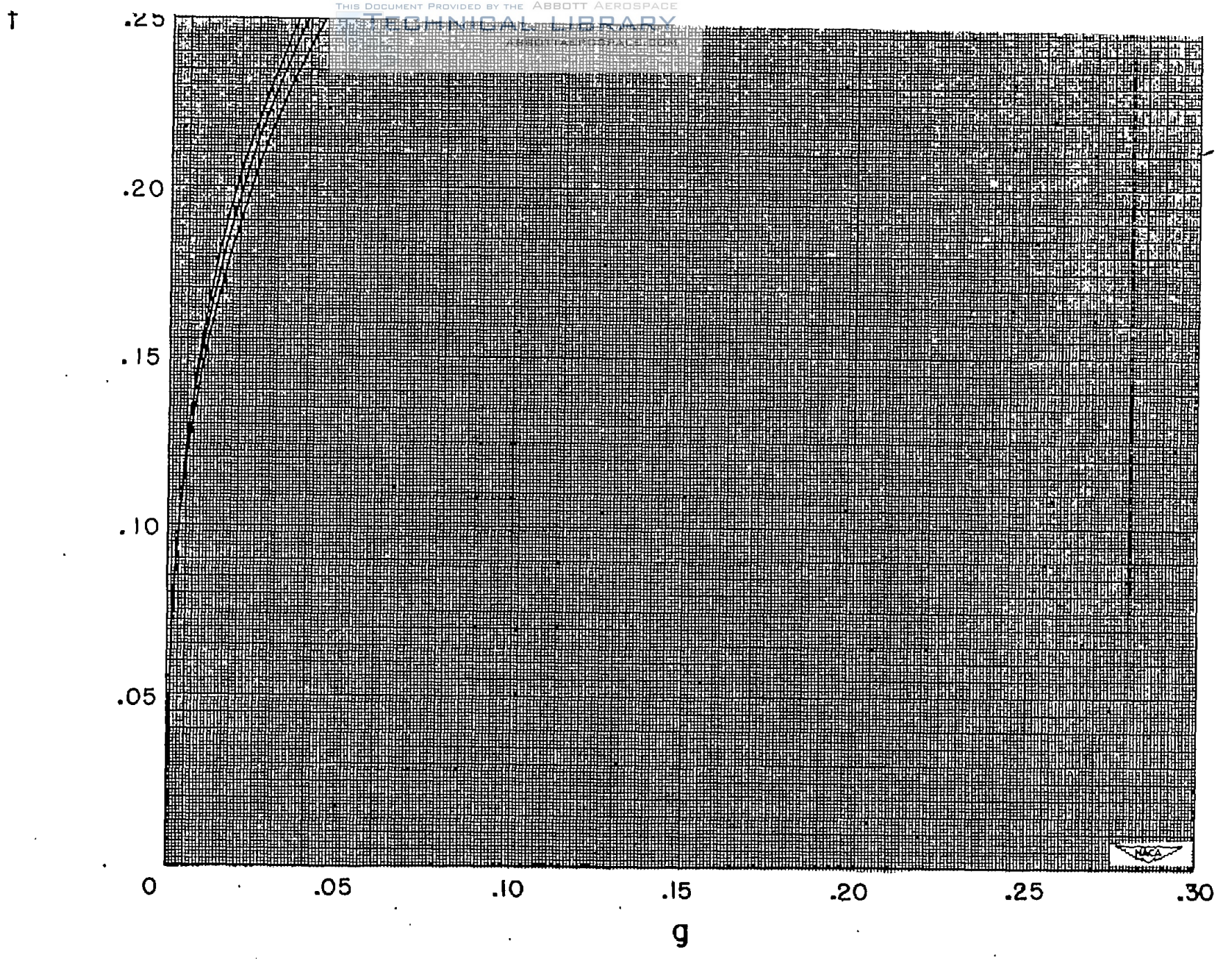

(b) Chart for finding f.

Figure 14. - Concluded. Chart for finding average velocity through blade channel.

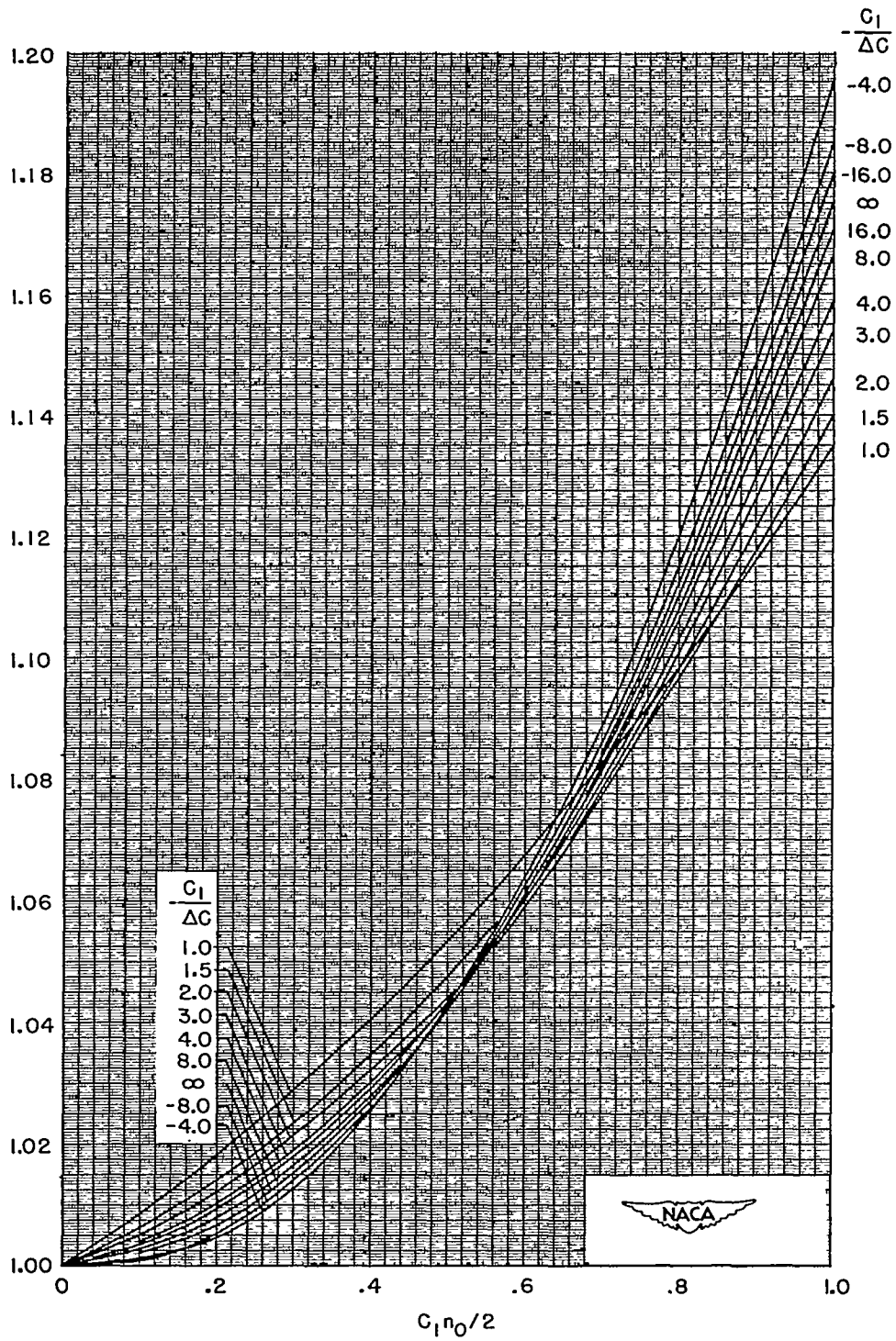

Figure 15.- Chart for finding J from channel width and blade curvature. (A 10-by-16-in. print of this figure is attached.)

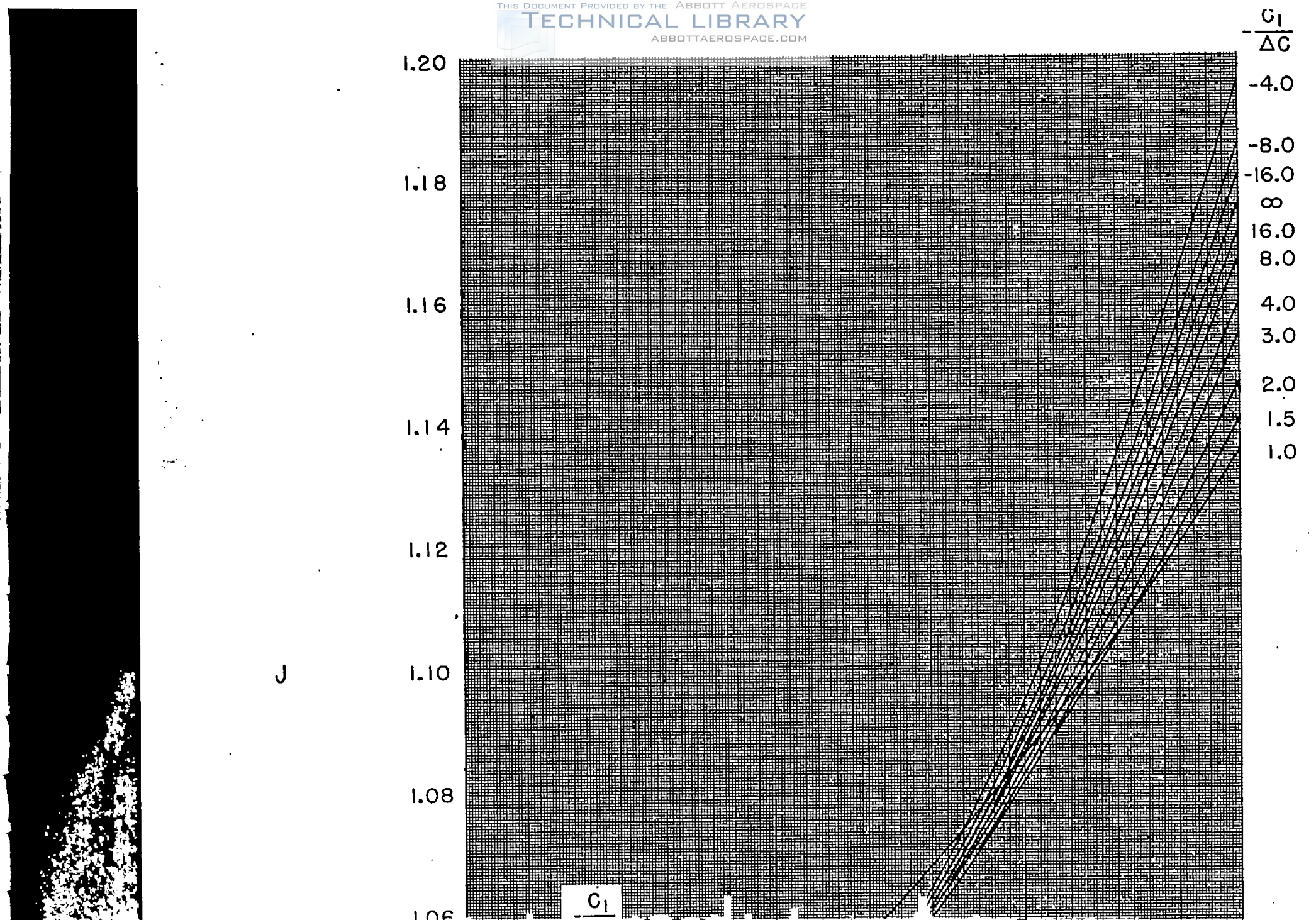

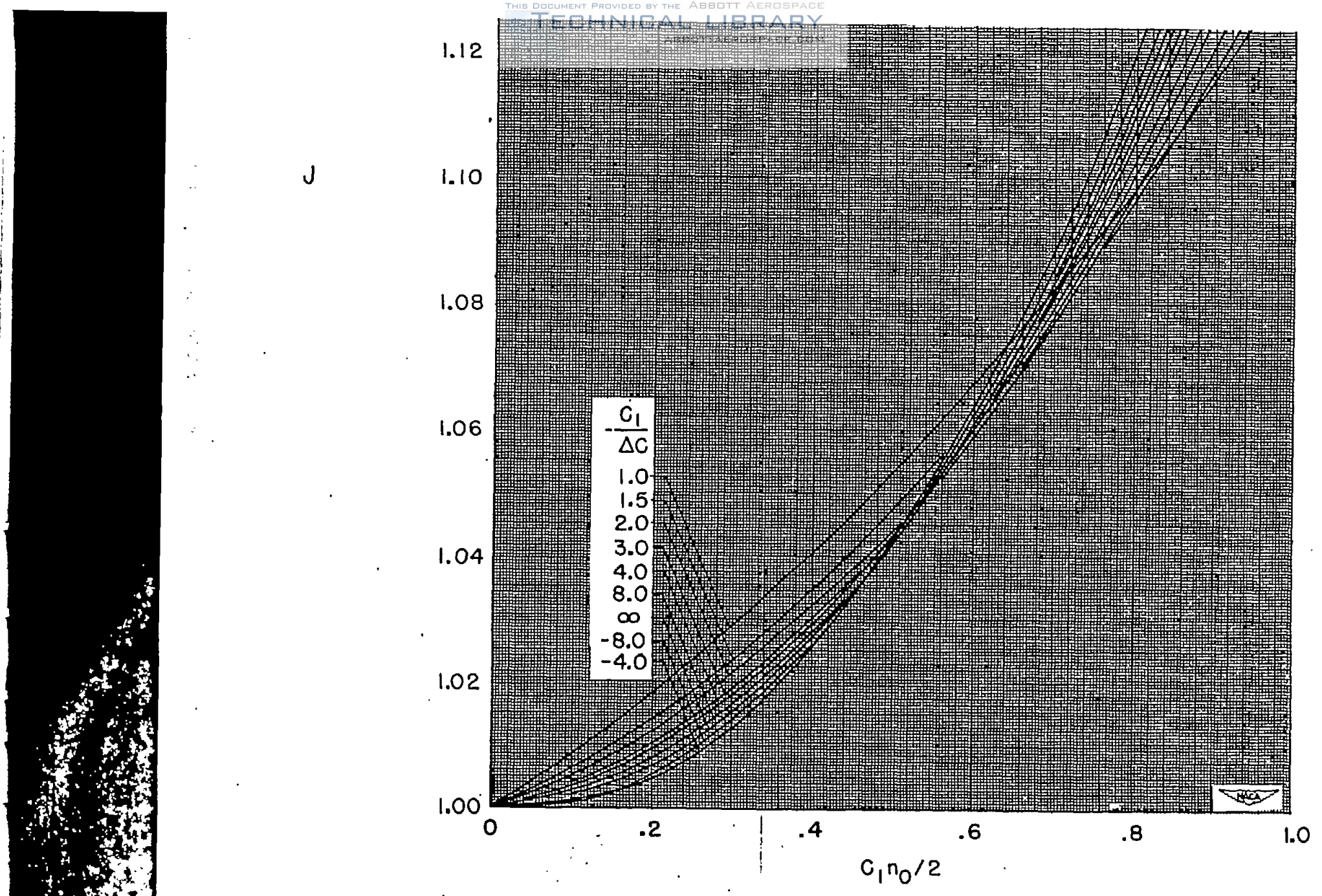

Figure 15. - Chart for finding J from channel width and blade curvature.

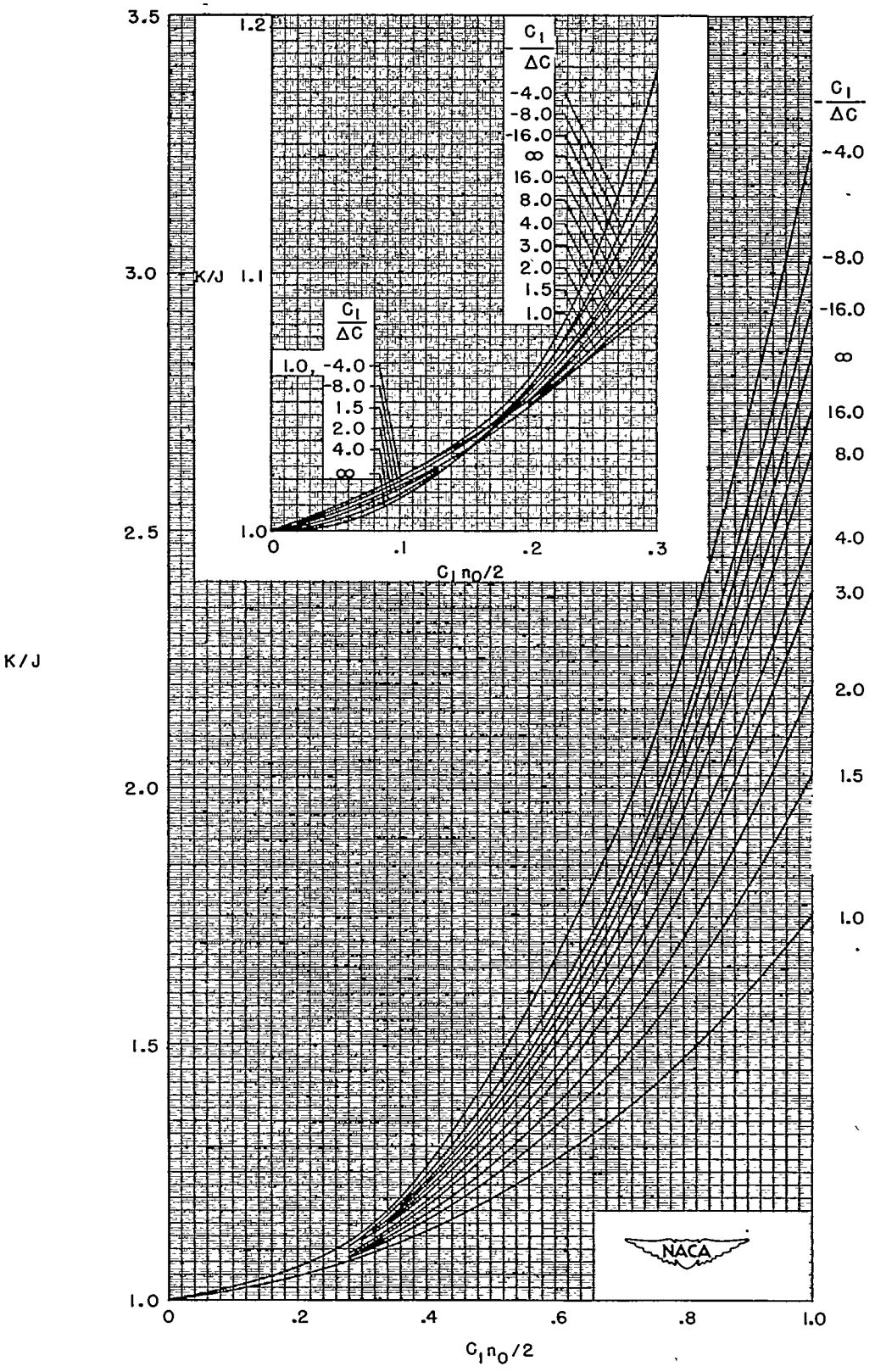

Figure 16.- Chart for finding K/J from channel width and blade curvature. (A 10-by-20-in. print of this figure is attached.)

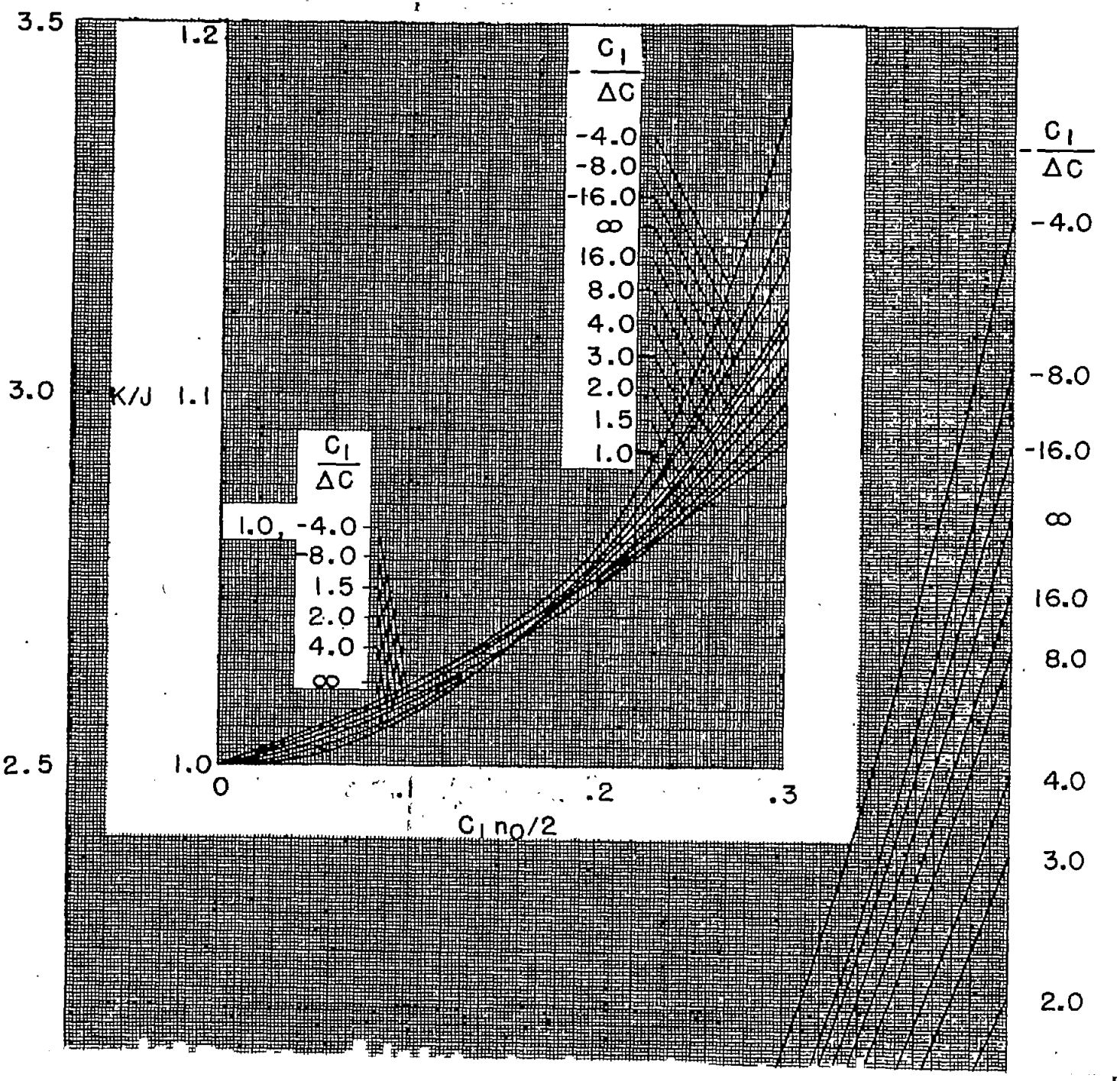

K/J

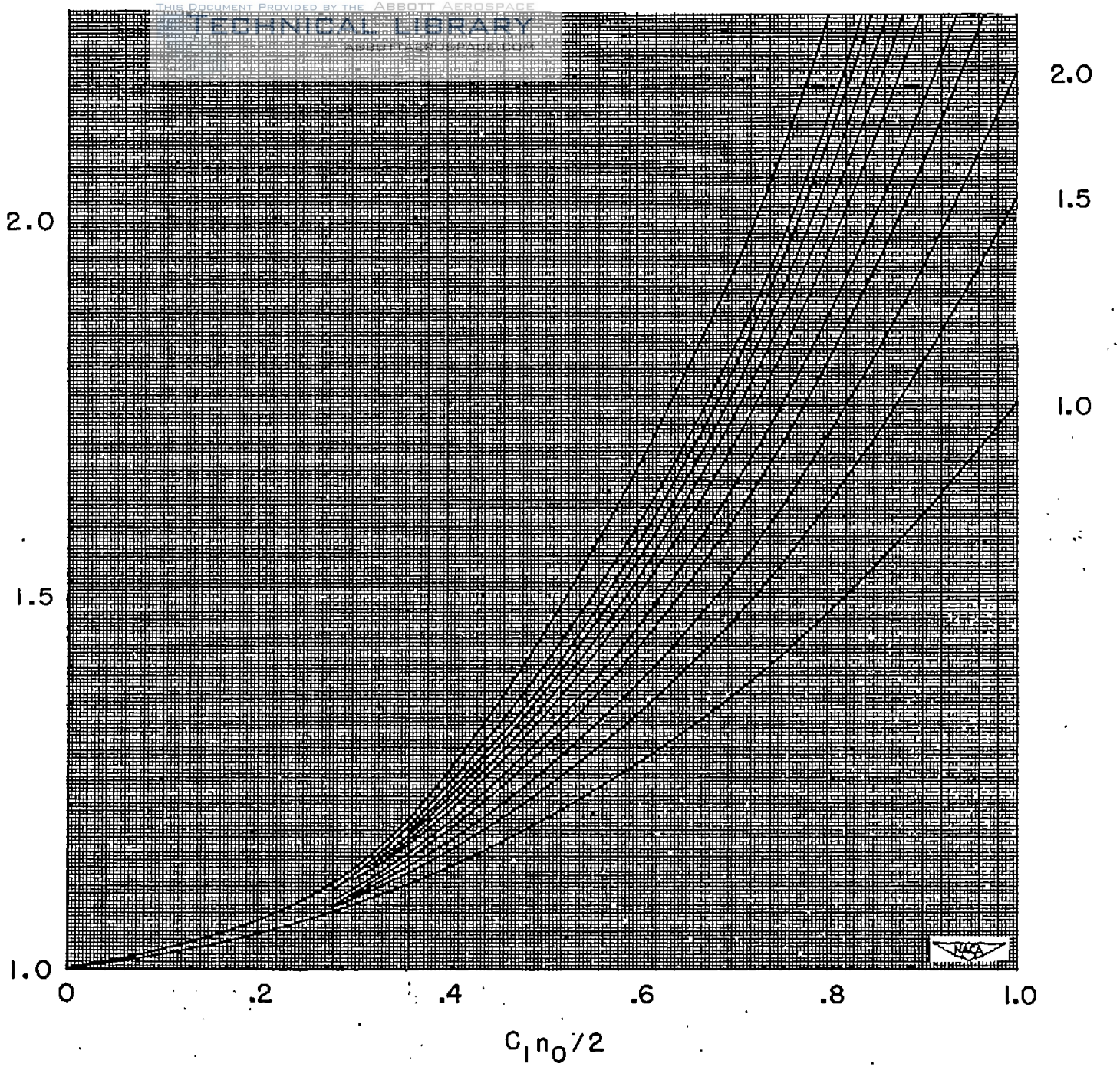

Figure 16. - Chart for finding K/J from channel width and blade curvature.

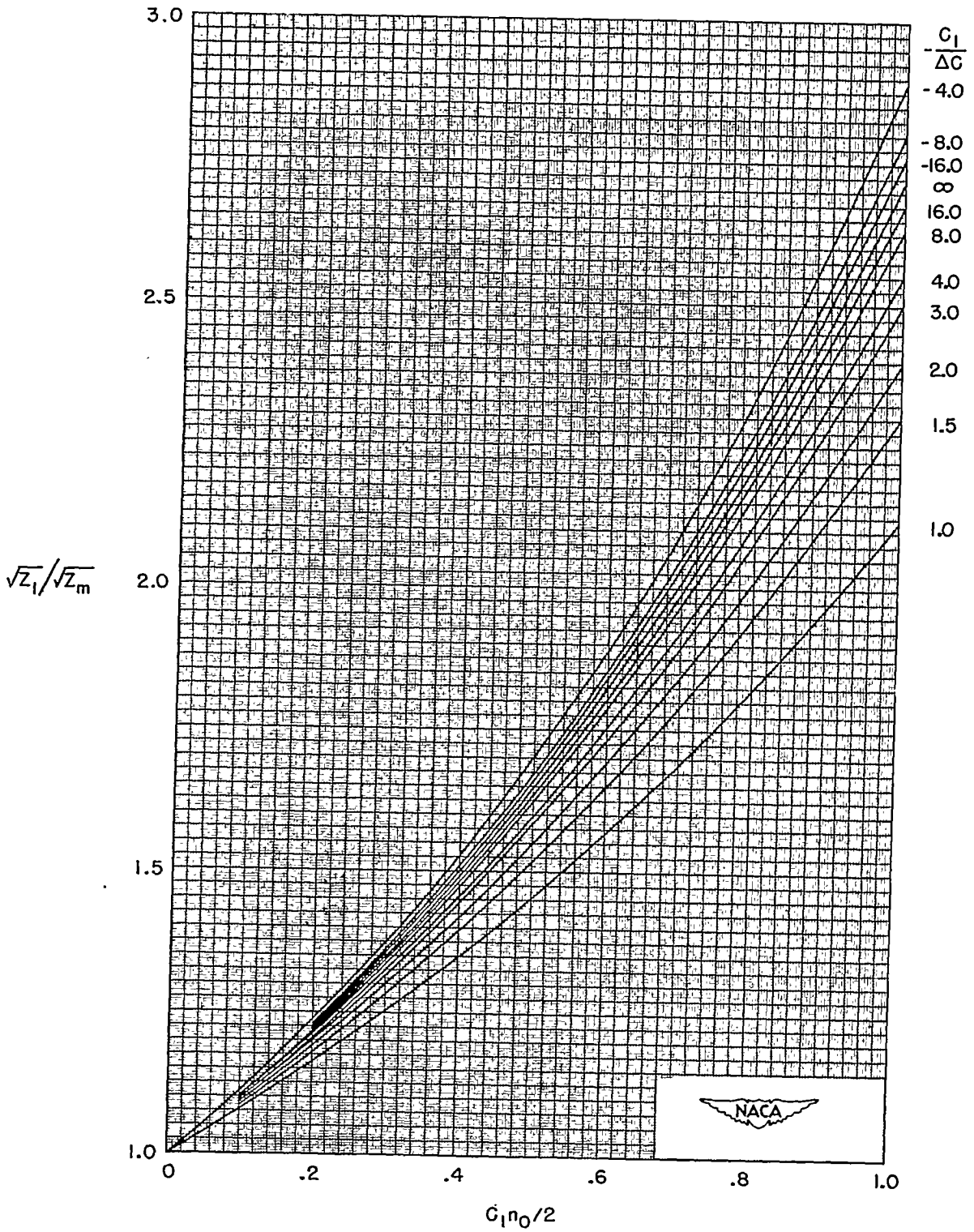

Figure 17.- Variation with channel width and blade curvature of ratio of velocities along blade suction surfaces to velocity at channel center. (A 10-by-16-in. print of this figure is attached.)

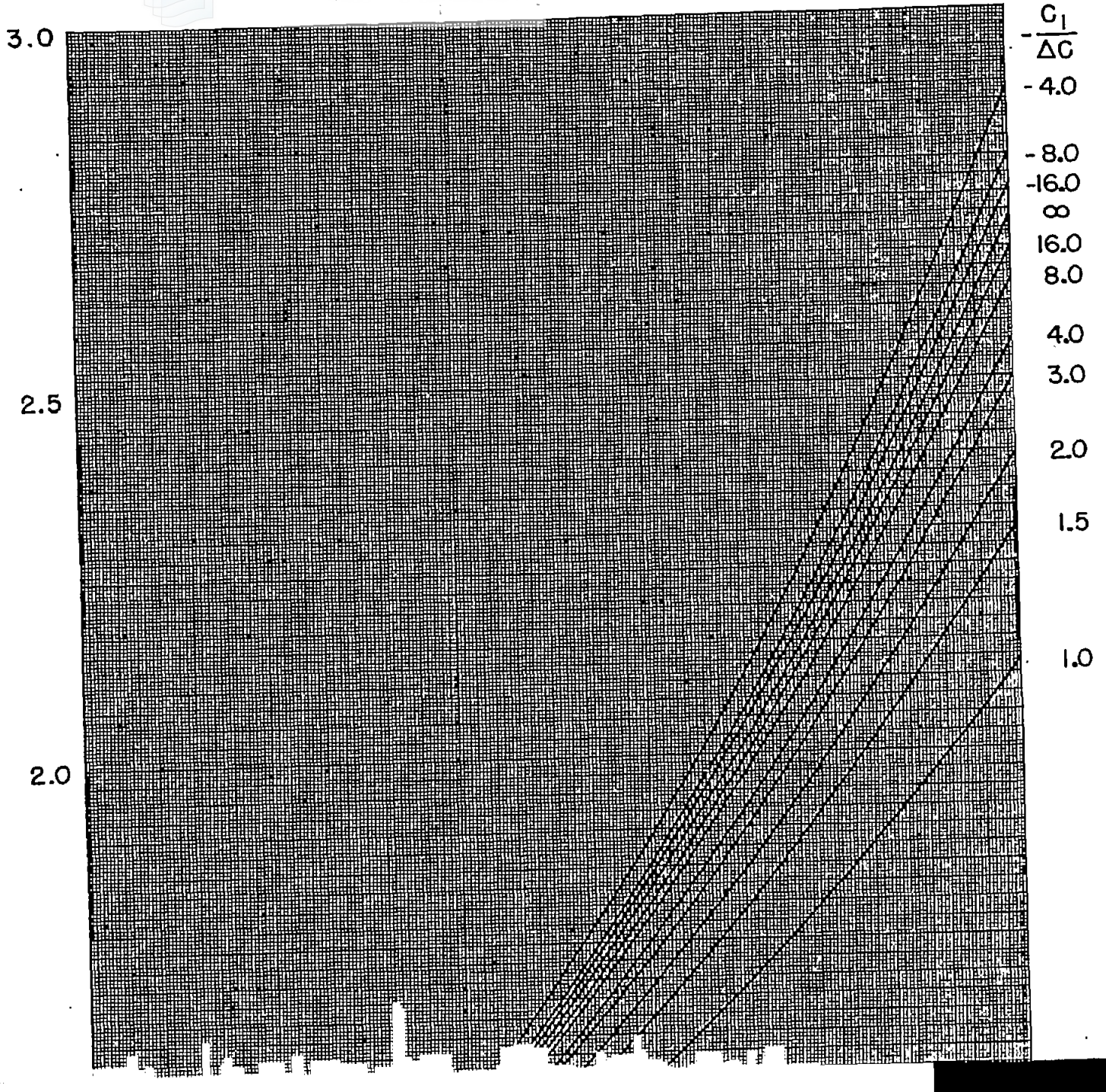

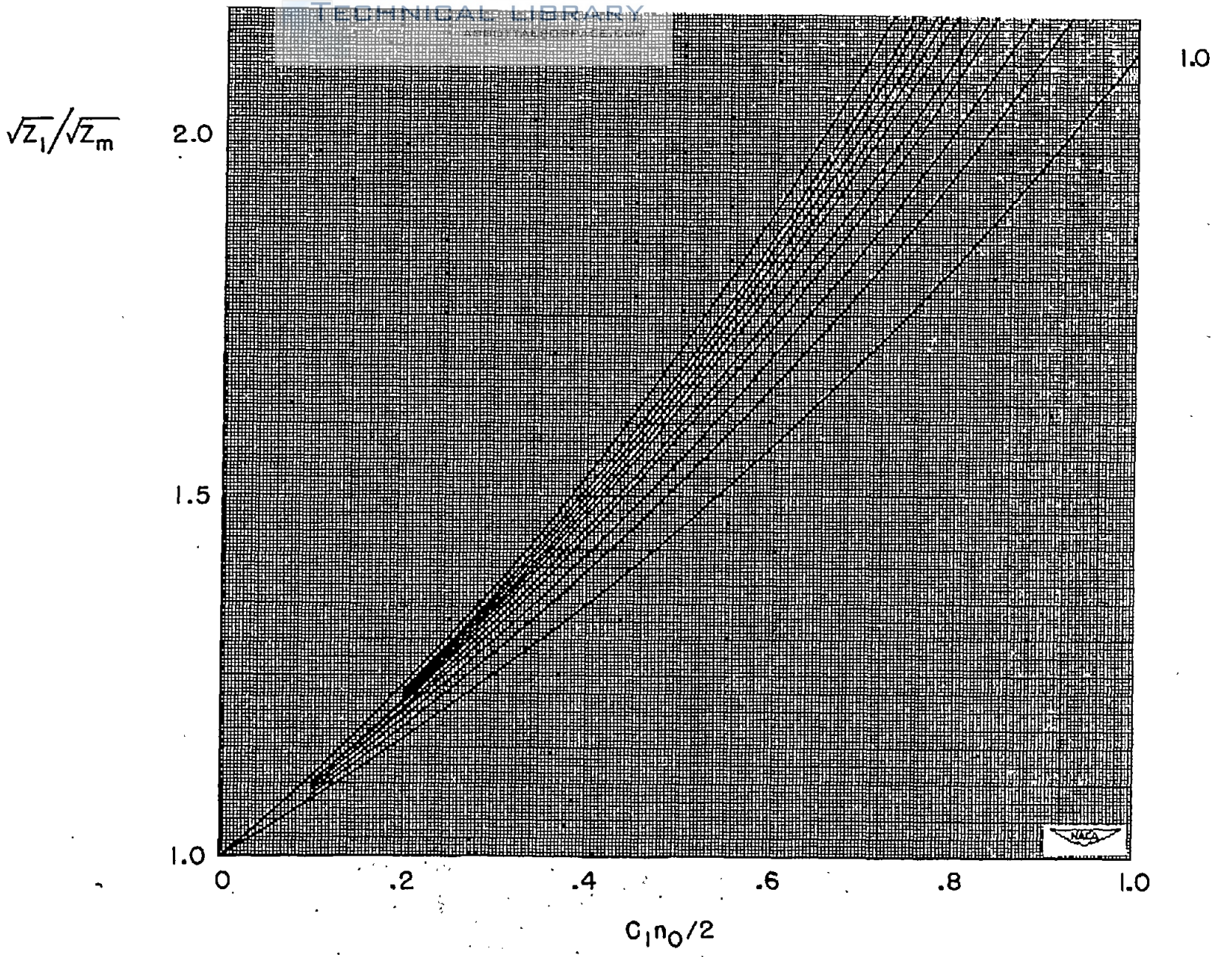

Figure 17. - Variation with channel width and blade curvature of ratio of velocities along blade suction surfaces to velocity at channel center.

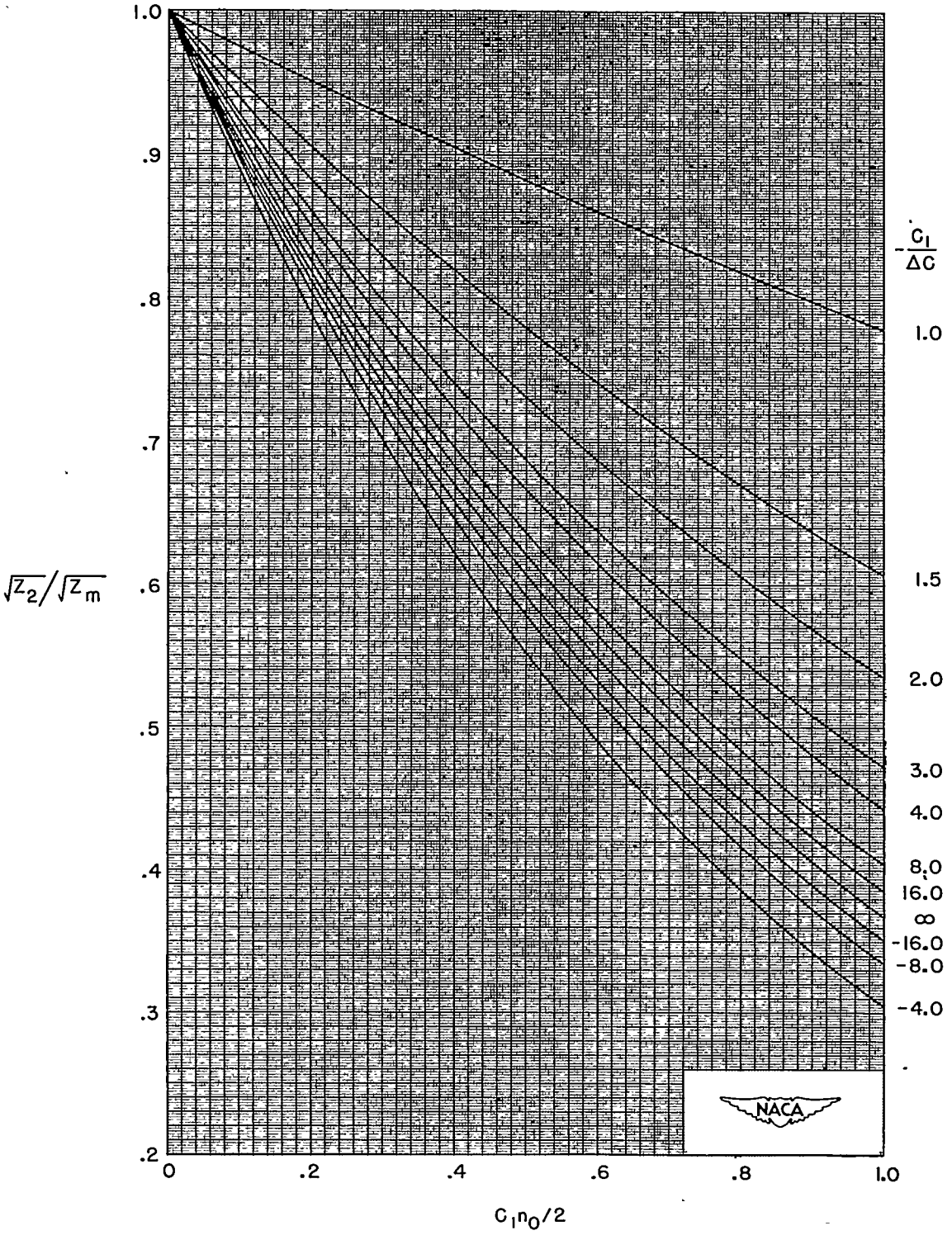

Figure 18.- Variation with channel width and blade curvature of ratio of velocities along blade pressure surfaces to velocity at channel center. (A 10-by-16-in. print of this figure is attached.)

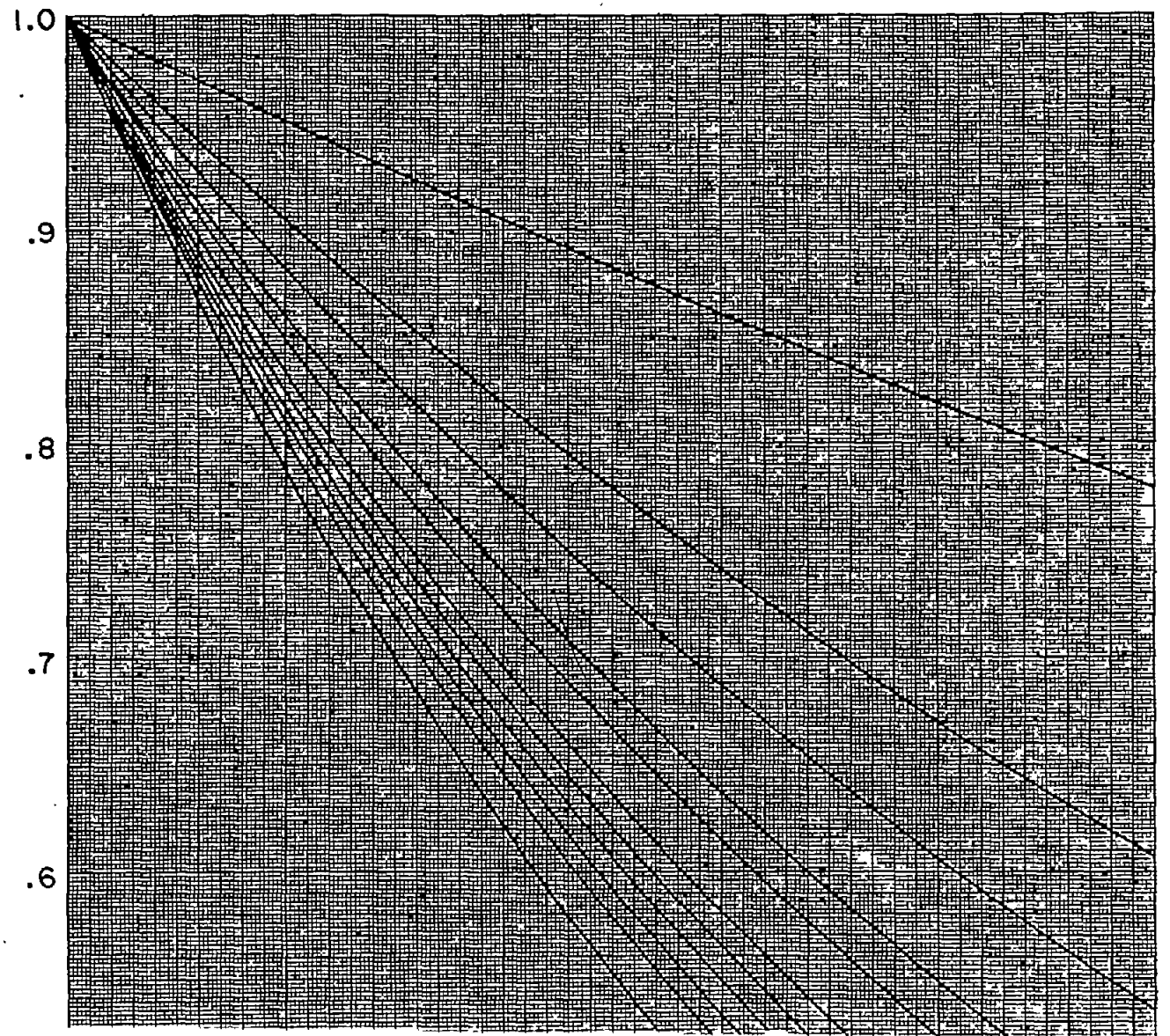

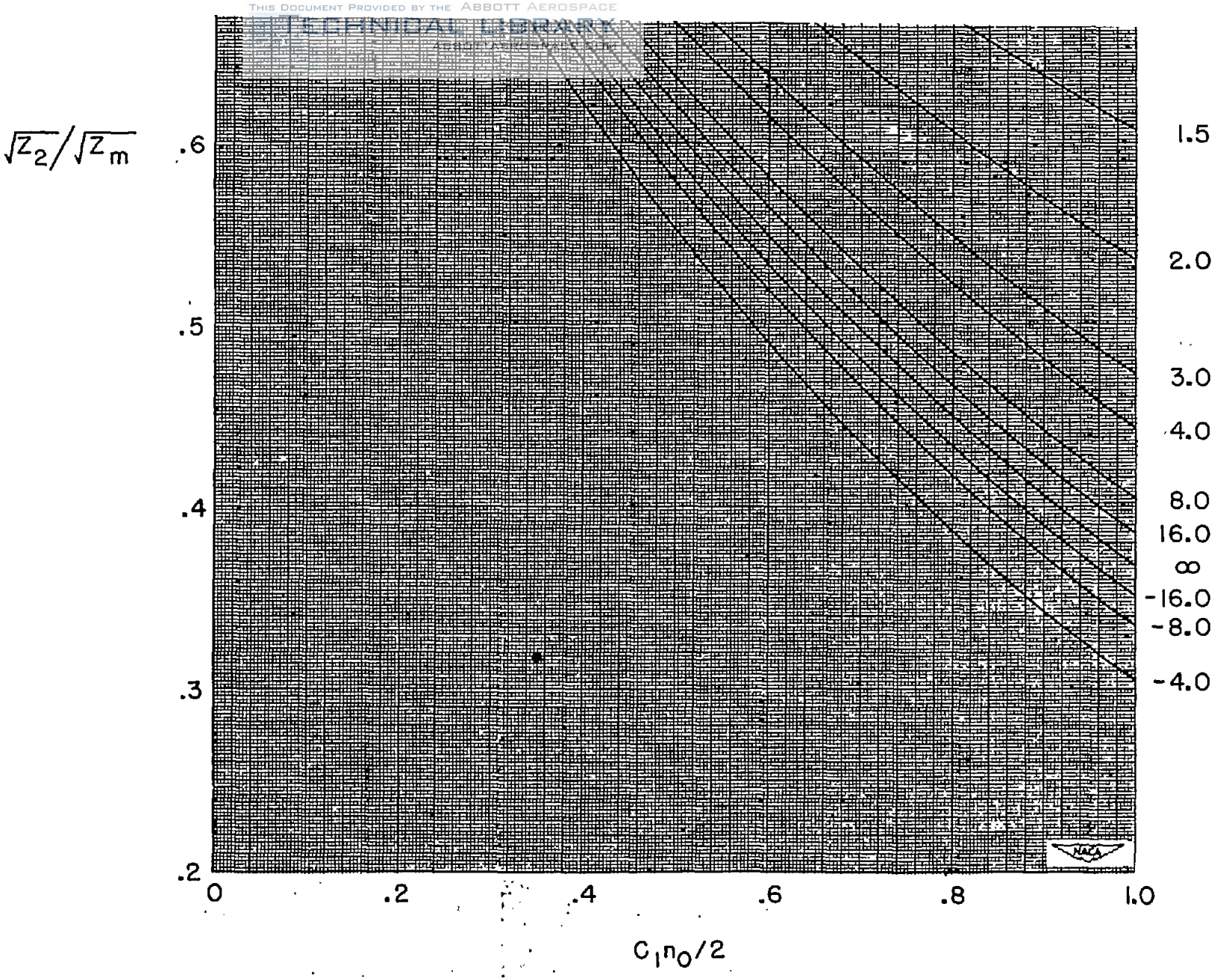

Figure 18. - Variation with channel width and blade curvature of ratio of velocities along blade pressure surfaces to velocity at channel center.

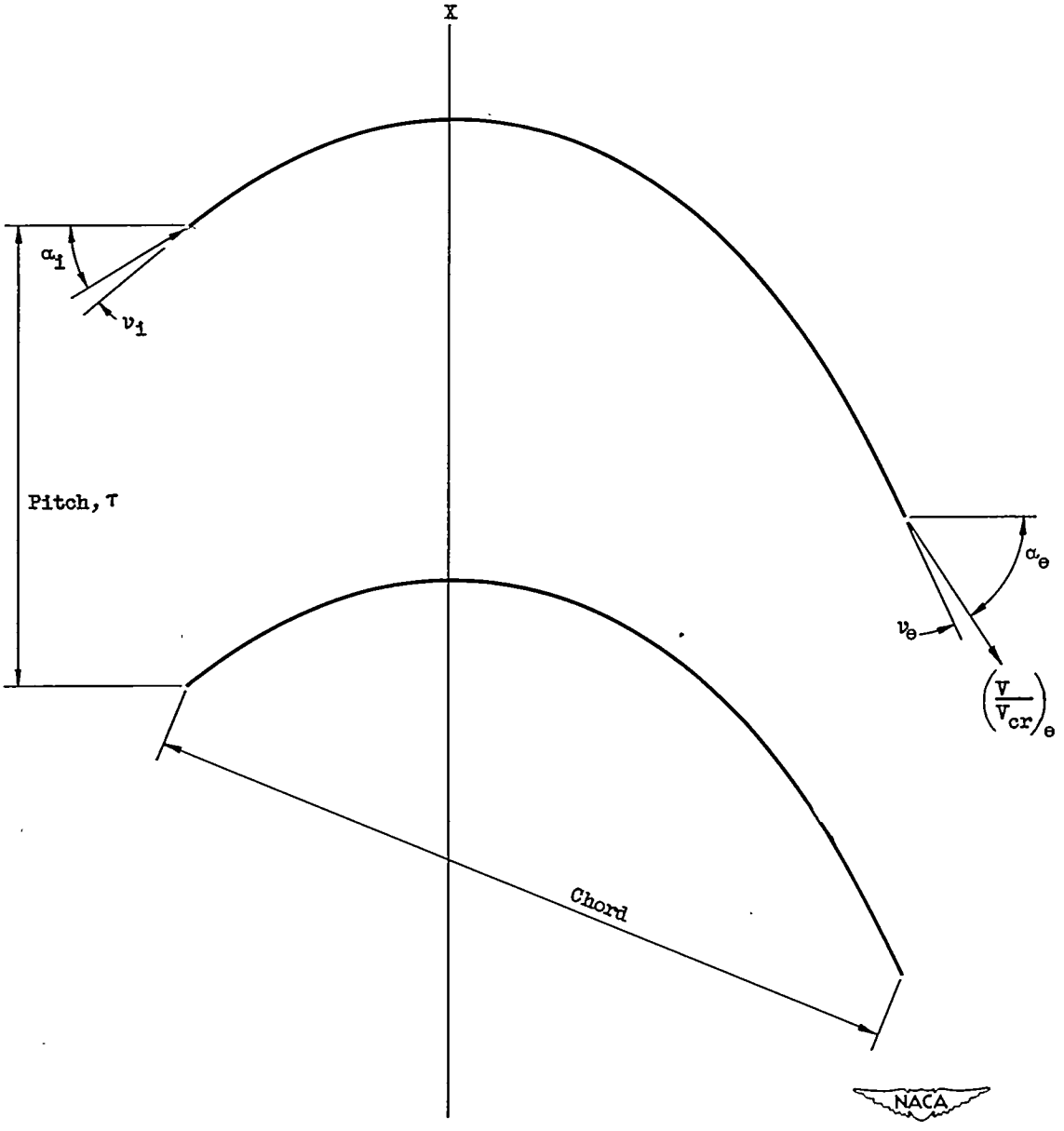

Figure 19.- Assumed camber lines.

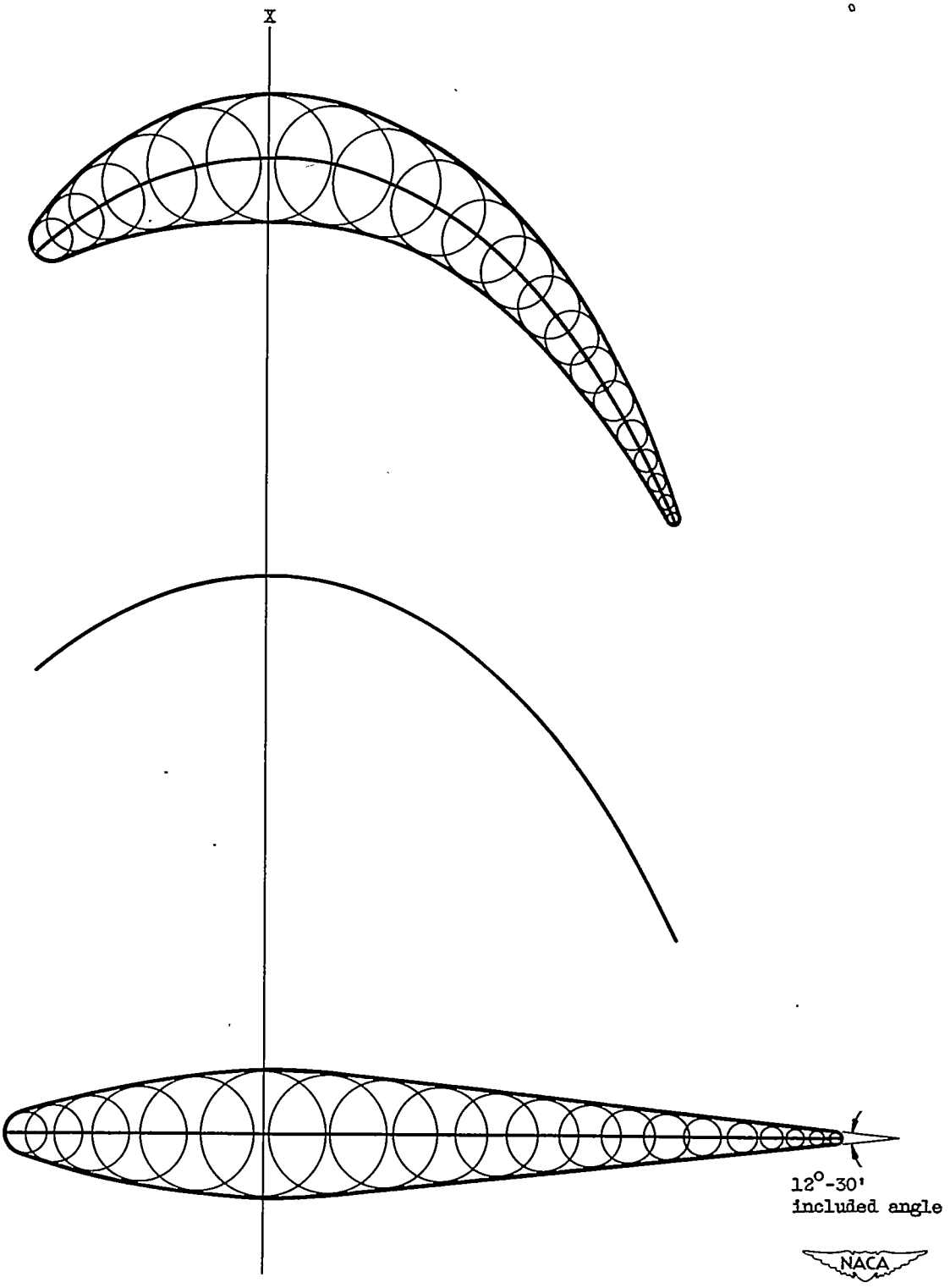

Figure 20.- Distribution of symmetrical airfoil on assumed camber lines.

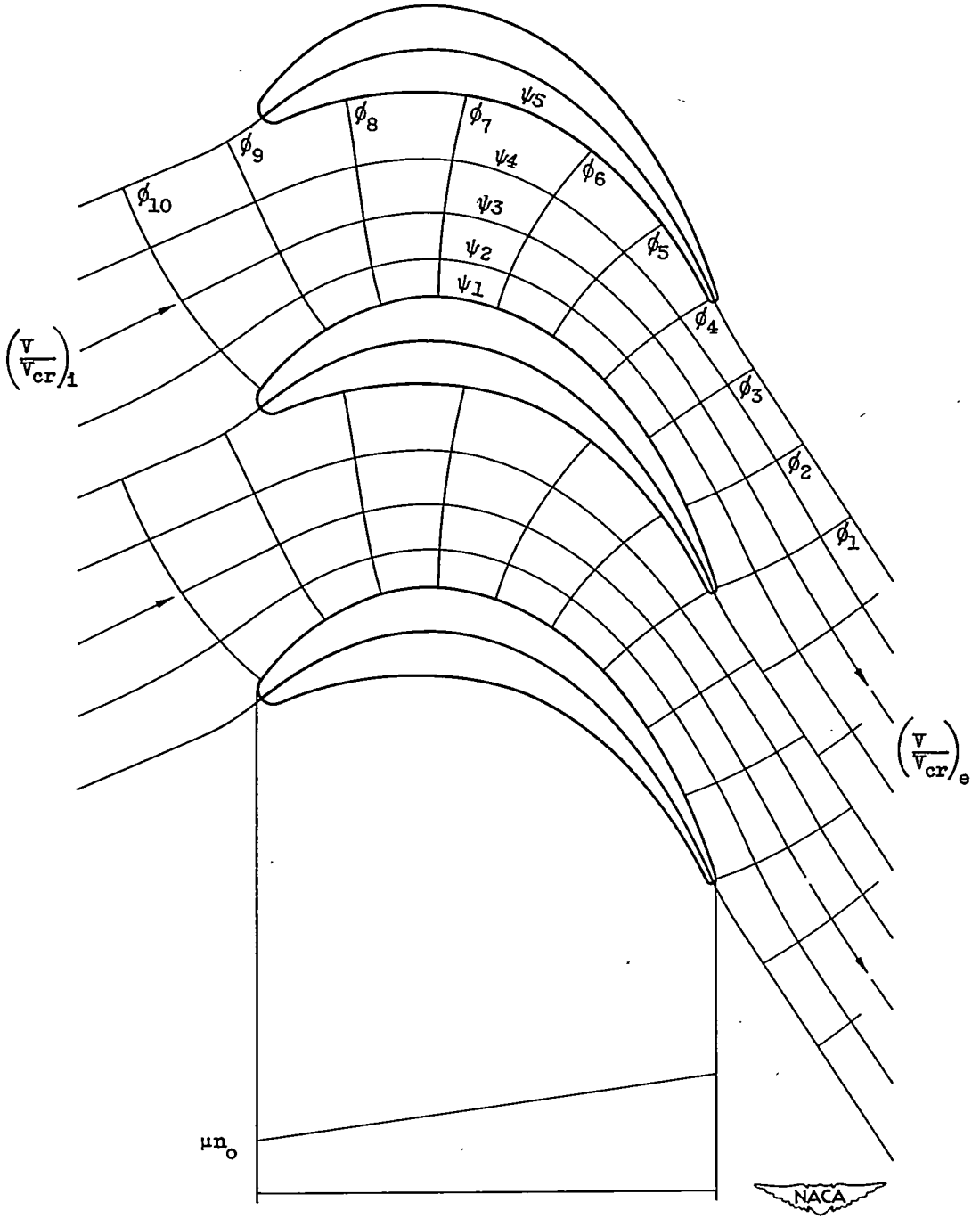

Figure 21. - Flow network in channel between blades and assumed distribution of weight-flow parameter.

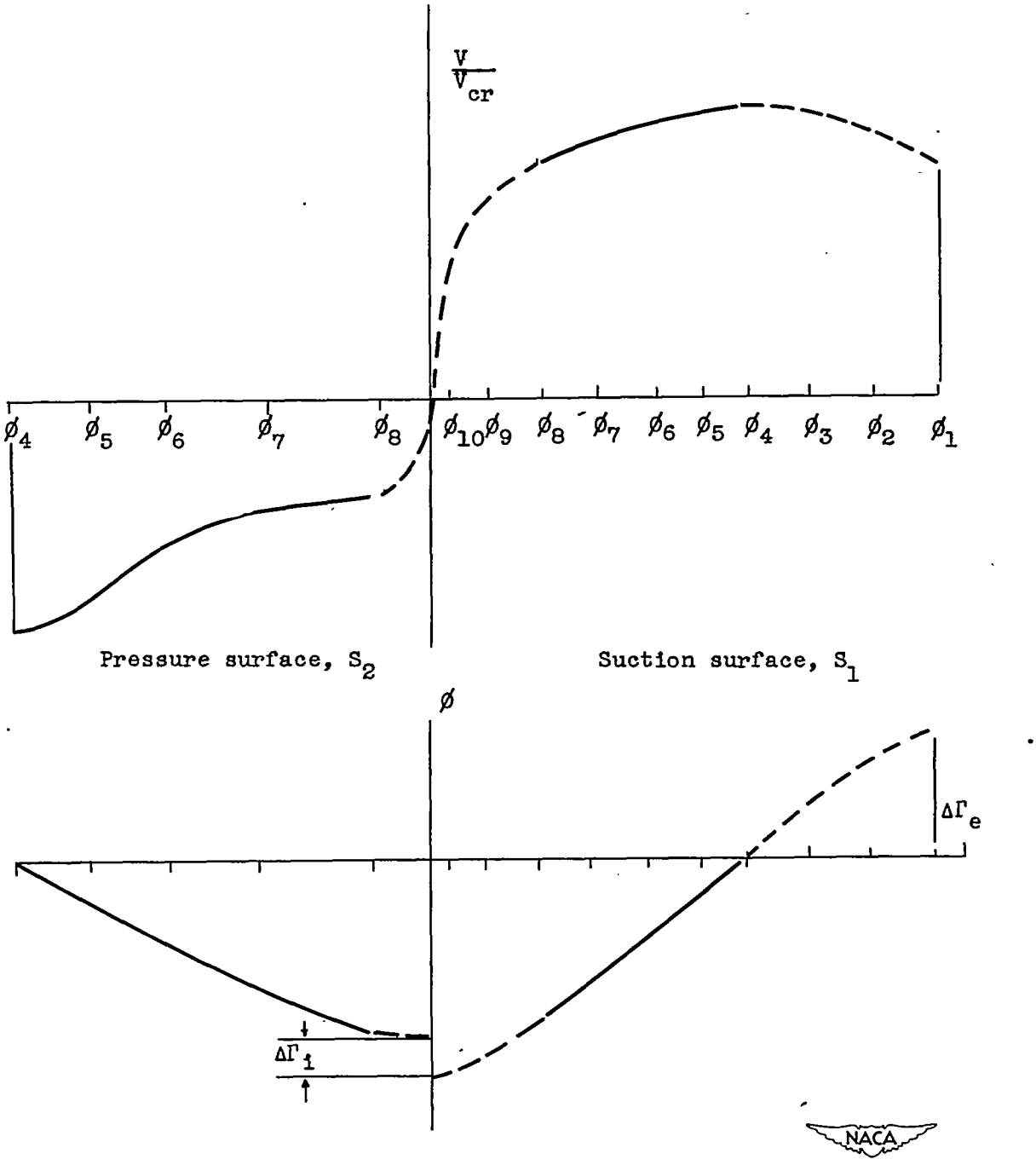

Figure 22.- Surface velocities and velocity potential. Dashed lines are based on an assumed boundary streamline.

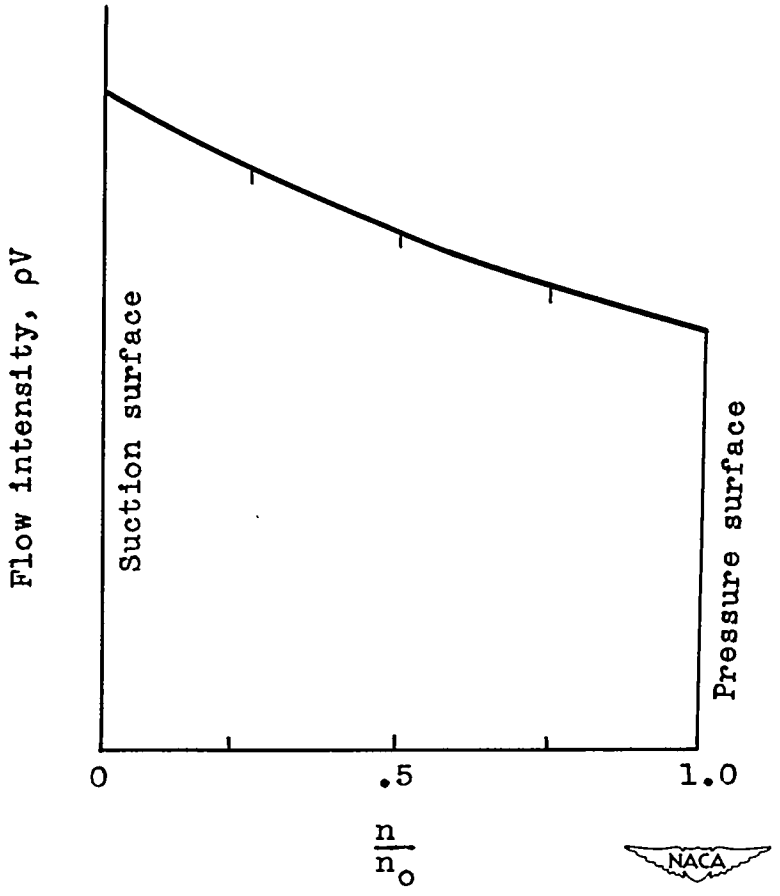

Figure 23.- Schematic diagram of variation of flow intensity with distance along velocity-potential line.

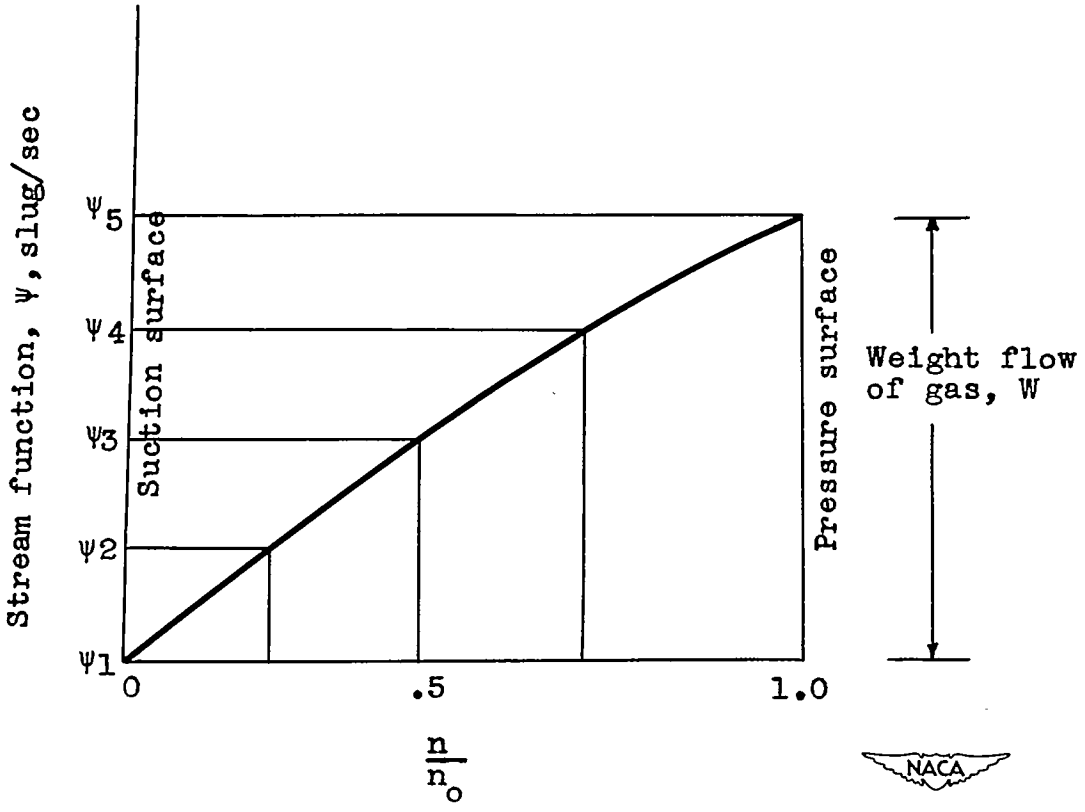

Figure 24.- Variation in stream function with distance along a velocity-potential line.